Palaeoceanographic and hydrodynamic variability for the last 47 kyr in the southern Gulf of Cádiz (Atlantic Moroccan margin): Sedimentary and climatic implications

Thomas D. Vandorpe, Stanislas Delivet, Dominique Blamart, Claudia Wienberg, Franck C. Bassinot, Furu Mienis, Jan Berend W. Stuut, David van Rooij

Received: 12 July 2022 | Revised: 26 October 2022 | Accepted: 1 November 2022

DOI: 10.1002/dep2.212

The Depositional Record
Open Access
A journal of the International Association of Sedimentologists
WILEY

ORIGINAL RESEARCH ARTICLE

Palaeoceanographic and hydrodynamic variability for the last 47 kyr in the southern Gulf of Cádiz (Atlantic Moroccan margin): Sedimentary and climatic implications

Thomas Vandorpe[1,2] | **Stanislas Delivet**[2] | **Dominique Blamart**[3] | **Claudia Wienberg**[4] | **Frank Bassinot**[3] | **Furu Mienis**[5] | **Jan-Berend W. Stuut**[5] | **David Van Rooij**[2]

[1]Flanders Marine Institute, Ostend, Belgium

[2]Department of Geology, Renard Centre of Marine Geology, Ghent University, Ghent, Belgium

[3]Laboratoire des Sciences du Climat et de l'Environnement, Unité Mixte CEA/CNRS/UVSQ, Avenue de la Terrasse, Gif-sur-Yvette, France

[4]MARUM – Center for Marine Environmental Sciences, University of Bremen, Bremen, Germany

[5]NIOZ – Royal Netherlands Institute for Sea Research, Den Burg, The Netherlands

Correspondence
Thomas Vandorpe, Flanders Marine Institute (VLIZ), Wanderlaarkaai 7, 8400, Ostend, Belgium.
Email: thomas.vandorpe@vliz.be

Funding information
Bijzonder Onderzoeksfonds; Deutsche Forschungsgemeinschaft, Grant/Award Number: He3412-18; Fonds Wetenschappelijk Onderzoek, Grant/Award Number: 1524713N

Abstract

X-ray fluorescence, grain-size and oxygen and carbon stable isotope measurements of a 33 m long piston core, recovered from the Pen Duick drift located at the foot of the prominent Pen Duick Escarpment (Atlantic Moroccan margin), are combined to decipher past oceanographic conditions. The data indicate that, similar to the northern Gulf of Cádiz, the Azores Front exerts a major control on the palaeoclimatology of the region. Contrasting the northern Gulf of Cádiz, where Mediterranean Outflow Water is the main water mass at similar water depths, the palaeoceanography of the studied area is mostly influenced by the amount of Antarctic Intermediate Water advected from the south. The density contrast between the Antarctic Intermediate Water and the overlying North Atlantic Central Water determined the strength of the prevailing internal tides and corresponding high current speeds, which drastically impacted the sedimentary record. The most notable impact is the presence of a 7.8 kyr condensed section (30.5–22.7 ka BP). The formation of the Pen Duick sediment drift was not just controlled by the strength of the bottom currents and the intensity of the internal tides, but also by the amount of (aeolian) sediment supplied to the region. Although variable, drift-growth phases seem to mainly occur during colder periods of the last glacial, that is Heinrich and Dansgaard-Oeschger events during Marine Isotope Stage 3 and late Marine Isotope Stage 2. These periods, characterised by increased aeolian dust supply and higher bottom currents, coincide with a phase of prolific cold-water coral growth and enhanced coral mound formation as recorded in numerous cores obtained from the southern Gulf of Cádiz. This implies that both records (on and off mound cores) are pivotal to provide the complete picture of the palaeoclimatic and palaeoceanographic conditions in the region.

KEYWORDS

aeolian dust, Antarctic Intermediate Water, Azores Front, bottom currents, cold-water corals, Pen Duick drift

1 | INTRODUCTION

Contourites are widespread over the world's ocean floor and are defined as sediments deposited and/or substantially reworked by the action of bottom currents (Heezen et al., 1966; Rebesco et al., 2014). They form sediment bodies of various morphologies and dimensions and are associated with erosive features, such as moats and furrows (Faugères & Stow, 2008; Faugères et al., 1999; Rebesco et al., 2014; Stow et al., 2002). The northern part of the Gulf of Cádiz is considered a natural laboratory for contourite research given the presence of an extensive contourite depositional system created due to the interaction of the Mediterranean Outflow Water (MOW) with the seafloor (palaeo)-topography (Brackenridge et al., 2018; Gonthier et al., 1984; Hernández-Molina et al., 2002, 2006, 2011; Llave et al., 2011, 2007b; Stow et al., 2013). The MOW contourite depositional system has been and continues to be studied intensively, along with the discovery and characterisation of numerous other small-scale contourite drifts (Chen et al., 2014; Hanebuth et al., 2015; Miramontes et al., 2016; Tallobre et al., 2016). Primarily, these drift deposits are controlled by enhanced bottom currents along pre-existing topographic obstacles. They are thought to hold crucial information on the climate-related variability of the local and regional circulation patterns (Chen et al., 2016; Hanebuth et al., 2015; Liu et al., 2019; Zhang et al., 2016).

In the southern Gulf of Cádiz, such small-scale drifts, covering areas in the range of several tens of square kilometres and all located along topographic obstacles, have been documented in the El Arraiche mud volcano province (EAMVP; Figure 1B; Vandorpe et al., 2014, 2016). Topographic obstacles, such as tectonic ridges or mud volcanoes (Vandorpe et al., 2016), enhance the ambient bottom-current flow (average velocities around 9 cm/s) reaching maximum velocities of 30 cm/s (Mienis et al., 2012); leading to the formation of contourite drifts. The combined interaction with internal tides is hypothesised to play a crucial role in establishing these elevated bottom currents (Vandorpe et al., 2016; Vitorino et al., 2010).

The water mass responsible for the formation of the EAMVP sediment drifts is still being debated. Several authors demonstrated the presence of Antarctic Intermediate Water (AAIW) at depths of 700–1,500 m (Louarn & Morin, 2011; Mienis et al., 2012; Vitorino et al., 2010) and assumed that this water mass was responsible for the formation of the contourite features (Vandorpe et al., 2016). Some studies even confirmed the presence of AAIW within the region during glacial times (Dubois-Dauphin et al., 2016; Eberwein & Mackensen, 2008). Recently, however, Lebreiro et al. (2018) studied a 5 m long sediment core (MVSEIS-TG2, hereafter called TG2; Figure 1A), located 30 km south of the study area and ascribed the presence of contouritic deposits within that core to the presence of a southward branch of the (upper) MOW during colder periods.

Both AAIW and MOW have a major influence on the global climate-ocean interhemispheric asynchronicity model (bipolar seesaw). The production of AAIW is higher during glacial periods due to increased ventilation of deep southern hemisphere water masses, providing a strong feedback to northern hemisphere coolings (Anderson et al., 2009; Jung et al., 2011; Skinner et al., 2010; Wainer et al., 2012). The MOW, on the other hand, provides a salt source to the intermediate depth layers of the Atlantic during glacial stages (Voelker et al., 2006). The injection of salt and heat facilitated the switch of the thermohaline circulation into an interstadial mode, bringing back warmer conditions (Rogerson et al., 2006, 2012). Both water masses may thus have a positive feedback on (northern hemisphere) cooling phases.

Even though the (millennial-scale) MOW variability has received a lot of attention during the last decades (Cacho et al., 2000; Lebreiro et al., 2018; Llave et al., 2006, 2007a; Lofi et al., 2016; Voelker et al., 2006), as opposed to the variability of the AAIW in the north Atlantic, there is an increasing need for the characterisation of intermediate ocean water mass dynamics, since they are an important feature of the Atlantic Meridional Circulation and global ocean circulation (Böhm et al., 2015; Freeman et al., 2015; Lynch-Stieglitz et al., 2007; Martrat et al., 2007). Only a limited number of studies have focussed on the variability of the AAIW within the western sub-tropical Atlantic (Freeman et al., 2015; Huang et al., 2014; Thornalley et al., 2011), but even fewer have focussed on the AAIW within the eastern sub-tropical Atlantic. Moreover, these studies mainly relied on neodymium isotope analysis from cold-water corals (CWCs; Dubois-Dauphin et al., 2016; Montero-Serrano et al., 2011), which often results in discontinuous chronostratigraphic records due to highly variable (intermittent) CWC reef growth (Frank et al., 2011; Wienberg et al., 2009, 2010; Wienberg & Titschack, 2017). To obtain a stratigraphic record at a regional scale, a combination of complementary sediment cores recovered from CWC mounds (aggrading mainly during more energetic conditions) and sediment drifts (deposited during less energetic conditions) seems to be a promising approach (Hebbeln et al., 2016; Van Rooij et al., 2011).

In the EAMVP, both CWC mounds (Hebbeln et al., 2019a; Vandorpe et al., 2017) and small-scale contourite drifts (Vandorpe et al., 2016) are present. The CWC mounds in the region have been studied extensively (Foubert et al., 2008; Hebbeln et al., 2019a; Vandorpe et al., 2017; Wehrmann et al., 2011), displaying

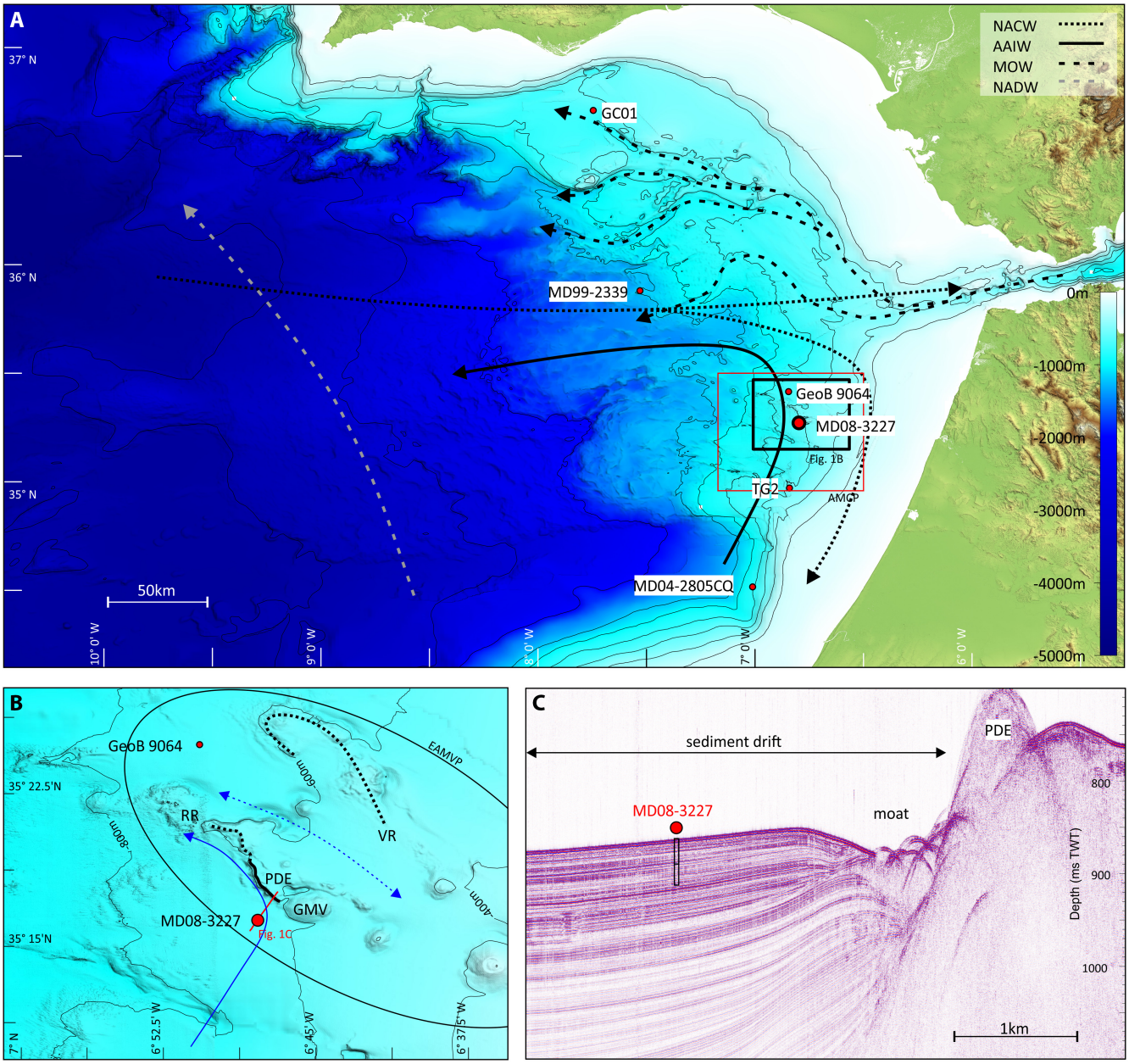

FIGURE 1 (A) Overview bathymetric map of the Gulf of Cádiz with indication of cores GC01 (Lebreiro et al., 2018), MD99-2339 (Voelker et al., 2006), GeoB 9064 (Wienberg et al., 2010), TG2 (Lebreiro et al., 2018) and MD04-2805CQ (Penaud et al., 2011) and the studied core MD08-3227. The bathymetric data are a collection of GEBCO, SWIM (Zitellini et al., 2009) and multibeam data acquired during surveys on board RV Belgica and RV Maria S. Merian (Hebbeln et al., 2015; Van Rooij et al., 2005). The Atlantic Moroccan Coral Province (Vandorpe et al., 2017) is indicated by a thin red square. (B) Bathymetric map of the surroundings of core MD08-3227 with indication of the El Arraiche Mud Volcano Province (EAMVP; Vandorpe et al., 2014). The blue arrow indicates the direction of the deflected bottom currents in the region, while the dashed blue double arrow indicates the direction of the internal tidal currents (Vandorpe et al., 2016). The red line indicates the location of the seismic profile. (C) Seismic profile, depth in milliseconds two-way travel time, across the Pen Duick Escarpment (PDE) and Pen Duick drift, with the location and subsurface depth of core MD08-3227 indicated. NACW, North Atlantic Central Water; AAIW, Antarctic Intermediate Water; MOW, Mediterranean Outflow Water; NADW, North Atlantic Deep Water; AMCP, Atlantic Moroccan Coral Province; RR, Renard Ridge; GMV, Gemini Mud Volcano; VR, Vernadsky Ridge.

intermittent growth phases, mainly during glacial periods (Frank et al., 2011; Wienberg et al., 2009, 2010). The small-scale contourite drifts in the area have received far less attention (Vandorpe et al., 2014, 2016). Core MD08-3227 potentially contains the optimal characteristics to decipher the temporal bottom-current variability as well as climate evolution of this key area. This core is ideally located to catch the presence of (glacial) intermediate water masses within the southern Gulf of Cádiz, given its current position at the interface between NACW (North

Atlantic Central Water) and AAIW, which is associated with internal tide activity (Martins & Vitorino, 2012). Moreover, this paper aims to advance the knowledge of the evolving climate of the southern Gulf of Cádiz since the late Marine Isotope Stage (MIS) 3 by constraining the (millennial-scale) sedimentation pattern of the Pen Duick drift.

2 | REGIONAL SETTING

The EAMVP (*ca* 35.25°N to 35°N and 6.5°E to 7°E) lies in the northern part of the Atlantic Moroccan Coral Province (Hebbeln et al., 2019a; Vandorpe et al., 2017), an area containing multiple topographic obstacles, including tectonic ridges, mud volcanoes and CWC mounds (Figure 1B). Two tectonic ridges, Renard Ridge and Vernadsky Ridge, oriented roughly NW-SE, are present within the EAMVP (Figure 1B) and are the result of a local compressive regime in an overall extensional setting (Flinch, 1993; Maldonado et al., 1999; Van Rensbergen et al., 2005). The local compressive setting also induced the dissolution of salt, originating from the allochtonous unit of the Gulf of Cádiz (Maldonado et al., 1999), in the subsurface, causing salt-tectonic forces and continued uplift of the ridges throughout the Quaternary (Perez-Garcia et al., 2011). These dissolved salts also fuelled the nine mud volcanoes of the EAMVP, some of which rise over 100 m above the surrounding seafloor. In addition, over 3,440 CWC mounds with heights ranging between a few metres and >50 m (median of about 20 m) dot the seafloor of the Atlantic Moroccan Coral Province seafloor (Figure 1B,C; Foubert et al., 2008; Hebbeln et al., 2019a). Today, these exposed mounds are covered by fossil CWCs. Also in the subsurface, numerous buried CWC mounds of the same dimensions have been discovered, indicating multiple periods of coral proliferation and mound initiation (Vandorpe et al., 2017). Radiometric dating revealed that CWC growth was most pronounced during glacial periods, with most of the coral communities declining since the onset of the Holocene (Frank et al., 2011; Wienberg et al., 2010).

Four distinct small-scale contourite drifts surround the Renard and Vernadsky ridges, while some of the mud volcanoes are also accompanied by drift deposits (Vandorpe et al., 2016). The Pen Duick drift developed at the foot of the Pen Duick Escarpment and the southern flank of the Gemini mud volcano, at depths of about 650 m, is the largest of the four drifts, covering about 30 km^2 (Figure 1B). Seismic stratigraphy indicated a Quaternary development with mainly interglacial depositional phases. The seismic stratigraphy of the Pen Duick drift differs from the northern Gulf of Cádiz drift deposits with mounded deposits only occurring in the Pen Duick drift from the Mid-Pleistocene Transition onwards (versus base Quaternary in the north) and main boundaries at MIS 9 and 15 (versus MIS 12 in the north) (Vandorpe et al., 2014).

The Atlantic Moroccan margin is influenced by five water masses (Louarn & Morin, 2011; Machín et al., 2006; Mienis et al., 2012): the North Atlantic Surface Waters (0 to *ca* 100 m), the NACW (100–600 m), the AAIW (600–1500 m), the MOW (Ambar et al., 2008; Cabecadas et al., 2002; Richardson et al., 2000) and the North Atlantic Deep Water (NADW, below 1500 m). The NACW is characterised by a decreasing vertical salinity and temperature gradient from about 36.4–35.6 and *ca* 18–12°C, respectively. The AAIW in the study area is characterised by low salinity (*ca* 35.6) and temperatures (*ca* 11°C), but by high nutrient values (Machín & Pelegrí, 2009; Vandorpe et al., 2016). In the vicinity of the EAMVP, the MOW forms a saline (36.1) and relatively warm (11.5°C) water mass occasionally present as meddies between 800 and 1,200 m water depth (Ambar et al., 2008; Carracedo Segade et al., 2015). Below 1,200 m, salinity and temperature further decrease to minimum values of around 35.5 and 8°C, respectively. These values are characteristic of the NADW (Louarn & Morin, 2011).

The modern sea-surface circulation pattern (surface mixed layer and NACW) in the southern Gulf of Cádiz is dominated by different branches originating from the Azores current (Eberwein & Mackensen, 2006; Machín et al., 2006). The northern branch flows northwards along the Iberian Peninsula and forms the Iberian poleward current (Carracedo Segade et al., 2015). The central branch enters the Gulf of Cádiz and experiences an anticyclonic recirculation towards the south (Machín et al., 2006). Part of this branch enters the Mediterranean Sea (Millot et al., 2006). The southern branch of the Azores current (Canary current) forms the present-day Azores front (Alves et al., 2002) and flows along the North West African Atlantic margin towards the south.

The AAIW is formed at sub-Antarctic latitudes and flows northwards, centred at around 800 m depths (Machín & Pelegrí, 2009). When encountering the MOW in the Gulf of Cádiz, the AAIW partly mixes with MOW and deflects to the west, losing its expression on the way (Figure 1A; Louarn & Morin, 2011). The MOW enters the Gulf of Cádiz through the Gibraltar Strait with very high velocities (>200 cm/s) and divides into different branches as a result of the Coriolis force and seafloor topographies (Figure 1A; Hernández-Molina et al., 2016; Iorga & Lozier, 1999). Due to eddy-generation, the MOW is able to reach the southern Gulf of Cádiz, mainly at depths between 800 and 1500 m (Ambar et al., 2008). Some authors also reported on a southern branch of the MOW, which

may spread as far south as the Canary Islands, albeit exhibiting seasonal variation (Lebreiro et al., 2018; Machín & Pelegrí, 2009). Finally, the NADW flows from south to north in the Gulf of Cádiz (Louarn & Morin, 2011).

The Pen Duick drift is under the influence of the AAIW and the NACW, both flowing from south to north in the EAMVP (Mienis et al., 2012; Vandorpe et al., 2016). For the NACW, this current direction contrasts with the generally accepted (southward) circulation pattern (Figure 1A). The ambient bottom current strength is on the order of 8–10 cm/s, although strong semidiurnal tidal currents occur as well. These originate at the interface between the NACW and the AAIW at about 600 m water depth, with peak velocities exceeding 30 cm/s (Mienis et al., 2012). Although seasonal upwelling is documented towards the north and south of the study area, upwelling processes are not specifically observed in the EAMVP (Mienis et al., 2012; Pelegrí et al., 2005). Seasonal changes of the equatorward alongshore wind regime, i.e. stronger during spring and summer, may result in stronger upwelling taking place during spring/summer, while weaker upwelling is noticed during autumn/winter (Cropper et al., 2014). As with the colder winter periods, during longer colder periods (glacials) these winds may have been less strong, diminishing the overall effect of upwelling in the region (Peliz et al., 2005).

3 | MATERIALS AND METHODS

The 3,320 cm long CALYPSO piston core MD08-3227 (35°16.28′N; 6°47.89′W, 642 m water depth, Figure 1) was collected during the R/V Marion Dufresne MD169 'MiCROSYSTEMS' cruise in July 2008. This study focusses on the top 1,800 cm because the stratigraphy could not be sufficiently resolved below this core depth. The core mainly consists of homogeneous grey to dark grey and brownish silty clays and clayey silts without clear macroscopic stratification (Van Rooij et al., 2008). No sharp contacts between facies are observed over the entire section studied (Van Rooij et al., 2008), except for the interval between 539 and 589 cm, which displays a rather sharp upper boundary (Figure 2). This interval contains pockets and lenses of poorly sorted coarse sand and coarse shell fragments (Van Rooij et al., 2008; Figure 2).

3.1 | Isotope analysis

The fraction >150 μm was used for oxygen (planktonic $\delta^{18}O$ values) and carbon (planktonic $\delta^{13}C$ values) stable isotope measurements on mono-specific samples of the planktonic foraminifer *Globigerina bulloides* at the Laboratoire des Sciences du Climat et de l'Environnement (LSCE) at Gif-Sur-Yvette (France). The samples were taken at an average spacing of *ca* 10 cm within the top 1,800 cm of the core. Between 15 and 30 specimens (size fraction 250–315 μm) were hand-picked and cleaned in an ultrasonic bath of reagent-grade methanol (3 s) to remove impurities. A first series of measurements was performed in 2010 using a Delta+ Isotope Ratio Mass Spectrometer (IRMS). The second series was performed in 2014 using the IsoPrime IRMS. The spectrometers were equipped with an automated line for the CO_2 preparation before analysis and were intercalibrated and standardised to the Vienna Pee Dee Belemnite (VPDB) using international carbonate standards NBS 19 and NBS 18 (Coplen, 1996). For NBS 19, the assigned values are $\delta^{18}O$ VPDB = −2.20 ‰ and $\delta^{13}C$ VPDB = 1.95 ‰, while for NBS 18, designated values are $\delta^{18}O$ VPDB = -23.01 ± 0.10 ‰ and $\delta^{13}C$ VPDB = −5.01 ± 0.03 ‰. All reported values are expressed relative to VPDB in the classical delta (δ) notation in per mil. Several levels within the core were measured with both methods to check for consistent results. During each run, 10 laboratory standards (Carrara marble) were run, and the uncertainties are based on their external reproducibility, being 1 standard deviation of 0.05 ‰ for $\delta^{18}O$ VPDB and 1 standard deviation of 0.03 ‰ for $\delta^{13}C$ VPDB.

Stable benthoni $\delta^{18}O$ and $\delta^{13}C$ values of the benthonic foraminifer *Cibicidoides pachyderma* were measured at an average core depth resolution of *ca* 10 cm. The analyses were only conducted over the top 1,600 cm. The measurements were also performed at the LSCE, using IsoPrime IRMS. The analyses were carried out on 2–4 specimens selected from the 250–315 μm fraction. When *C. pachyderma* was absent within this fraction, measurements were performed using specimens >315 μm in size.

3.2 | Sediment geochemistry and grain size

To obtain the elemental composition of the sediments at 1 cm resolution, the core was analysed using the AVAATECH XRF core scanner at the Royal NIOZ (Texel, The Netherlands). The XRF core scanner uses energy-dispersive fluorescence radiation to measure the chemical composition of the sediment as element intensities in total counts or counts per second (Tjallingii et al., 2010). The measured element intensities depend on the element concentration in the sediment but also on matrix effects, physical properties, the sample geometry and hardware settings of the scanner (Röhl & Abrams, 2000; Tjallingii et al., 2007, 2010). After cleaning and preparation of the archived half of the core surface which was then covered with SPEXCerti Ultralene® foil, the core was measured at

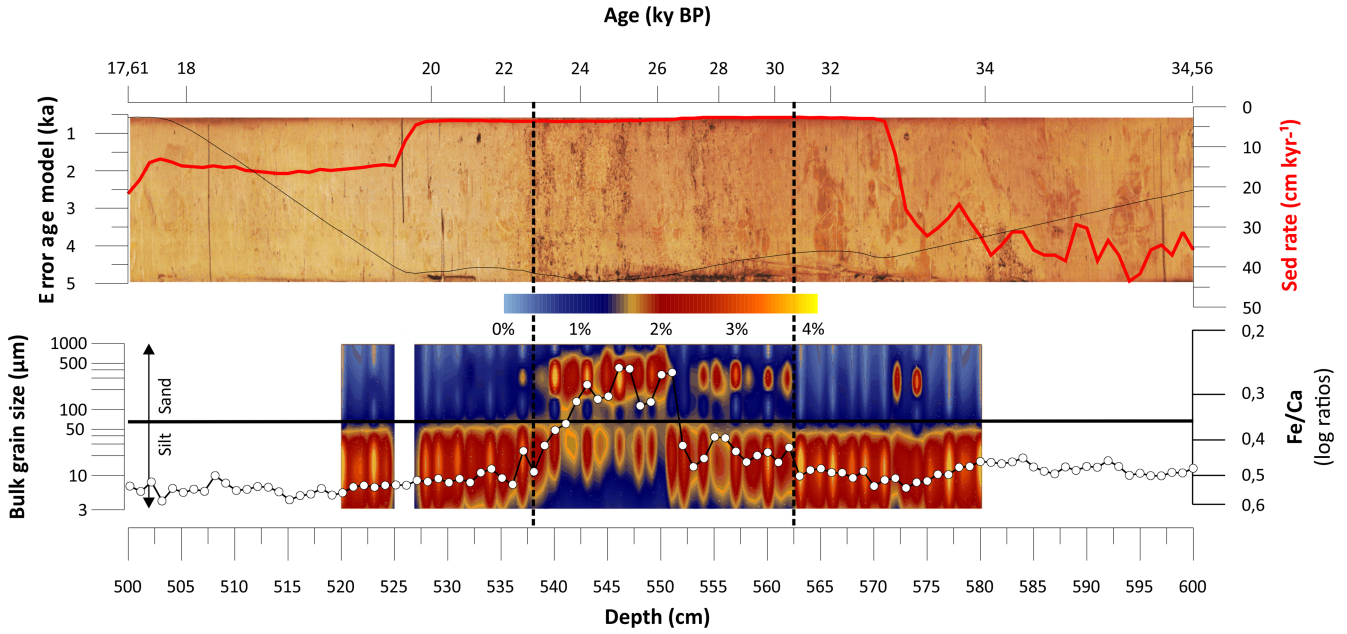

FIGURE 2 Overview of the condensed section (dashed black lines) within core MD08-3227. Upper panel: core picture between 500 and 600 cm core depth modified in terms of saturation, contrast and temperature to optimise the condensed section visualisation. The sedimentation rate (Figure 3) and error on the age model are superimposed. Lower panel: gridded bulk grain-size data (Malvern Mastersizer; grid display) along with the XRF log(Fe/Ca) ratio (white dots). No grain-size data were obtained between 526 and 527 cm. Grain-size axis is logarithmic, the boundary between sand and silt is indicated. The upper *X*-axis indicates the age, while the lower one displays core depth.

both 10 and 30 kV. Log-ratios of two elements measured by XRF core scanning can be interpreted as the relative concentrations of two elements and minimises the effects of down-core changes in sample geometry and physical properties (Weltje & Tjallingii, 2008). Each measurement was performed over an area of 1.2×1 cm using 30 s integration time.

The core was sub-sampled at irregular intervals based on the XRF data obtaining an average sample spacing of about 5 cm. The samples were sieved using mesh sizes of 63 and 150 µm. Grain-size analyses were carried out at the University of Ghent on the upper 1,250 cm of the core, using the sediment fraction below 63 µm. The analyses (N = 245) were performed using a Micromeritics Sedigraph III, providing information on the relative grain-size distribution between 2 and 63 µm. Before analysis, the removal of the biogenic carbonate fraction was performed using a twofold 1 mol/l acetic acid wash, each time followed by a distilled water wash. The biogenic silica (dissolving within the upper 1,000 m of the water column) and organic fractions (relatively remote from any source of organic matter) were considered negligible. Samples were then stirred using a rotating wheel in a 0.2% sodium hexametaphosphate solution for at least 24 h before measurement. From these measurements, the sortable-silt fraction (average within the 10–63 µm interval) was calculated. All 61 grain-size classes identified by the Sedigraph measurements, belonging to the silt fraction, have been used in an endmember modelling, an analysis performing a deconvolution on subpopulations of the grain-size spectrum (Weltje, 1997). To obtain the endmembers, the 'Emmageo v0.9.7' scripts of Dietze and Dietze (2019) have been used in R (version 4.2.1).

The interval between 520 and 580 cm core depth was further analysed for bulk grain-size distribution using a Malvern Mastersizer 3000 at the Department of Geology (Ghent University). Bulk grain size was measured at a resolution of 1 cm from samples ranging from 3 to 6 mg. Samples were boiled in a hydrogen peroxide solution to remove traces of organic matter, and to assist in dispersion of the particles. Boiling was continued until the reaction could no longer be visually detected, usually about 15 minutes. One millilitre of 0.2% sodium hexametaphosphate solution was added to each sample prior to measurement to limit the formation of particle aggregates (McCave & Hall, 2006). Samples were introduced into the Malvern using a Hydro MV module with a stirrer speed of 2,500 rpm. A continuous ultrasonic bath was set at 2% to avoid breaking the foraminiferal material. Each sample was run three times, each time using a 12 s integration interval, with the results averaged.

In order to verify the co-variance of several sets of proxies, correlation coefficients have been calculated using the statistical program 'SPSS Statistics 27' and its 'dimension reduction' option. These coefficients are mentioned in the discussion.

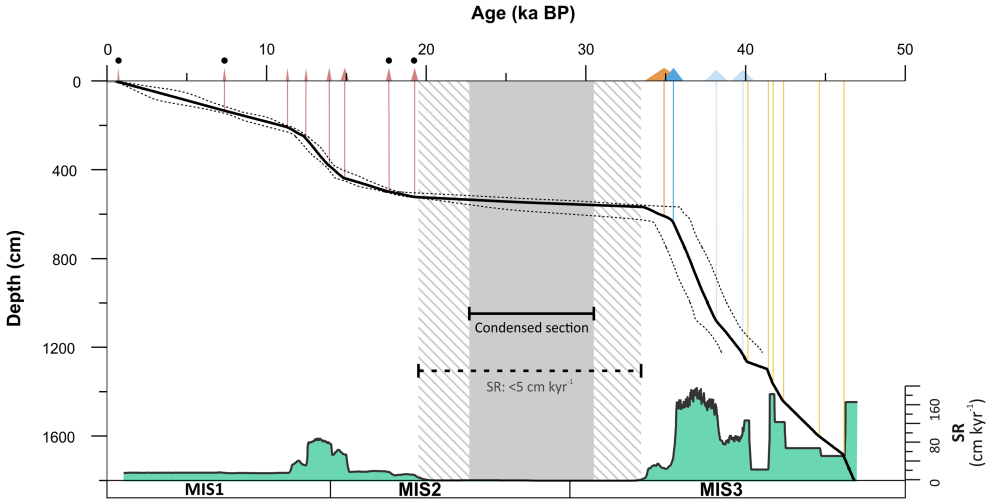

FIGURE 3 Age-depth (ka BP) model for core MD08-3227. The red triangles indicate AMS^{14}C-ages (Waelbroeck et al., 2019; this study), all other triangles are tie-points described in Waelbroeck et al. (2019) with the base of the triangles indicating their uncertainty. Black dots above the red triangles indicate AMS^{14}C-ages obtained within the framework of this study. The orange triangle is a tie-point based on extrapolation of sedimentation rates, the dark blue triangle is based on the alignment of δ^{18}O values from *Globigerina bulloides* to NGRIP data and the two light blue triangles are tie-points based on the alignment of δ^{18}O values from *G. bulloides* to core MD99-2339. The six yellow lines are tie-points beyond 40 ka BP and are established within this study based on the alignment of δ^{18}O values from *G. bulloides* to core MD99-2339. The solid black line is the resulting age model, while the dashed lines indicate the 2σ uncertainty margins of the model. The calculated sedimentation rates are displayed in green at the bottom of the figure.

3.3 | Age model

An age model of core MD08-3227 covering the past 40 kyr was first presented by Waelbroeck et al. (2019) and is based on eight accelerator mass spectrometry (AMS) radiocarbon (^{14}C) ages and four tie-points (Figure 3, Table 1). The dating was performed at the Poznan Radiocarbon Laboratory (Poland) using samples of mono-specific planktonic foraminifera *Globigerinoides ruber* white or *G. bulloides* and at ETH Zurich (Switzerland) using mixed samples of *G. ruber* white and *G. bulloides*. The AMS ^{14}C ages were calibrated (ka BP) using the Bayesian calibration program MatCal (Lougheed & Obrochta, 2016) and the IntCal13 calibration curve (Reimer et al., 2013), a reservoir age correction of $R = 530 \pm 100$ years was applied (calibration method described in detail in Waelbroeck et al., 2019). Two of the four tie-points are alignments of δ^{18}O values from *G. bulloides* to core MD99-2339, a well-dated core taken 95 km north-west of core MD08-3227 (Figure 1; Voelker et al., 2006). One tie-point results from aligning δ^{18}O values from *G. bulloides* to NGRIP data, while the last tie-point is based on extrapolation of glacial sedimentation rates of *ca* 154 cm/kyr. To extend the age model beyond 40 ka BP, for this study, a correlation between planktonic δ^{18}O values of *G. bulloides* of cores MD08-3227 and MD99-2339 was established. Six additional tie-points were used and linear interpolation between them applied to extend the age model back to 47 ka BP (Figure 3).

3.4 | Power spectrum

In order to detect statistically relevant temporal variations within the dataset, a time series analysis has been performed (Alonso et al., 2021; Hoogakker et al., 2011; Pardo-Iguzquiza & Rodríguez-Tovar, 2011). A multivariate Lomb-Scargle periodogram (Scargle, 1982) has been applied on the MD08-3227 core data. The Lomb–Scargle periodogram (Lomb, 1976; Scargle, 1982) is a well-known algorithm for detecting and characterising periodicity in unevenly sampled time-series (VanderPlas, 2018). An important factor in the Lomb–Scargle periodogram is the amount of data; more data will yield statistically more relevant periodograms, which will be reflected in the statistical confidence level (VanderPlas, 2018). The statistical confidence levels are inversely related to the probability of a 'false alarm' of the spectral peaks. Spectral peaks with confidence levels below 95% are not considered.

The periodograms (Figure 4) for planktonic δ^{18}O values (indicator of palaeoclimate cycles) and sortable silt (indicator for bottom current cycles) have been constructed using Matlab-scripts. Both proxies contain insufficient data points (101 for sortable silt and 56 for planktonic δ^{18}O values) in the post-condensed section period to calculate meaningful periodograms for this interval (their peaks do not surpass the 50% statistical confidence level). Therefore, only the pre-condensed section periodograms (MIS3) are considered. In these, peaks not followed by minima below 90% confidence level are

TABLE 1 AMS ^{14}C ages and tie-points of core MD08-3227 (calibration method) described in detail in Waelbroeck et al. (2019).

Lab code	Species	Core depth (cm)	^{14}C age (years)	Error (1σ) (years)	Calibrated median age (years BP)	Error (1σ) (years)	Calibrated age range (1σ) (years BP)
POZ-75177	*Globigerina ruber* (white)	5	1280	70	706	90	794 to 633
POZ-75178	*G. ruber* (white)	135	7040	50	7364	90	7458 to 7268
ETH-84711	*G. bulloides* + *G. ruber*	210	10473	44	11374	220	11589 to 11562
ETH-84712	*G. bulloides* + *G. ruber*	250	11113	54	12403	170	12573 to 12361
ETH-84713	*G. bulloides*	380	12697	66	13913	130	14046 to 13768
ETH-84714	*G. bulloides*	439	13239	72	14850	300	15147 to 14648
Poz-68942	*G. bulloides*	500	15250	110	17642	200	17841 to 17473
Poz-68943	*G. bulloides*	525	16750	150	19280	220	19497 to 19048
	Tie points	571[1]			34873	1200	
		623[2]			35448	660	
		1080[3]			38170	730	
		1225[3]			39850	750	
		1280[4]			40600		
		1380[4]			41882		
		1473[4]			42808		
		1517[4]			43432		
		1659[4]			45669		
		1816[4]			46940		

Note: 1—Based on extrapolation of glacial sedimentation rates of *ca* 154.4 cm/kyr; 2—alignment of δ^{18}O values from *Globigerina bulloides* to NGRIP data; 3—alignments of δ^{18}O values from *G. bulloides* to core MD99-2339; 4—based on a correlation between planktonic δ^{18}O values of *G. bulloides* of cores MD08-3227 and MD99-2339.

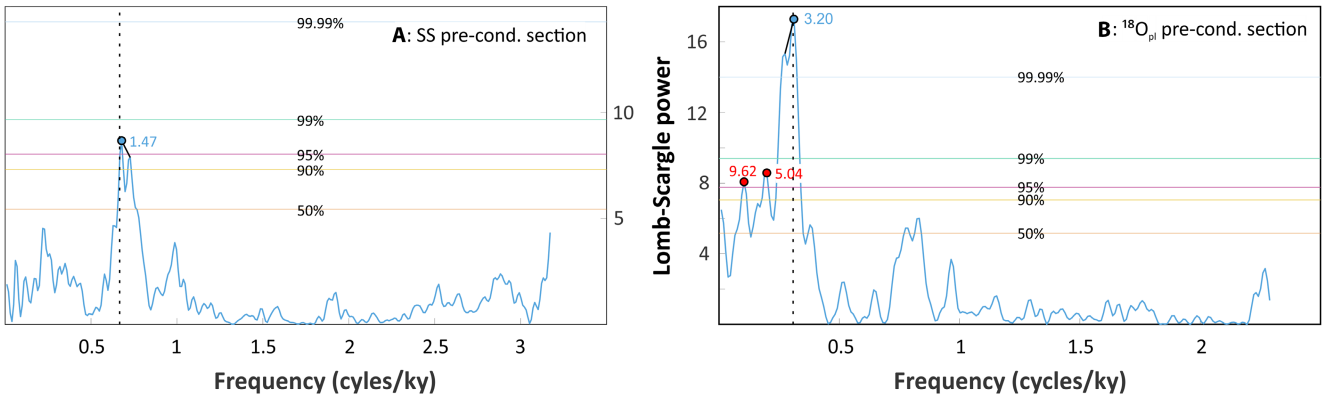

FIGURE 4 Time series analysis based on the Lomb-Scargle periodograms for mean sortable silt (SS) and planktonic δ^{18}O values for the pre-condensed section period of core MD08-3227. Confidence levels are indicated in each plot in colour, and peaks not surpassing the 95% barrier are not considered. The vertical black dashed lines indicate the maximal frequency which allows a minimum of four cycles within the considered time period. Frequencies exceeding this maximum, although surpassing the 95% confidence level, are presented as red dots. Solid black lines connect peaks not separated by minima below 90% confidence level.

considered as the same peak and the highest peak of the group is considered the dominant cycle. Such groups of peaks are connected by a solid black line in Figure 4. Additionally, peaks which appear less than four times in the time frame of the dataset (6.5 kyr for sortable silt and 11.5 kyr for planktonic δ^{18}O values) are considered statistically insufficient. This threshold can be calculated by dividing the time frame by four (the minimum number of required occurrences) and is indicated by a vertical dashed line in Figure 4.

FIGURE 5 Multi-proxy record of core MD08-3227 versus age (considering the last 47 kyr). For comparison, the stable isotope records of the core MD99-2339 (Voelker et al., 2006) is displayed (for core location see Figure 1). Rapid climate events are indicated (Younger Dryas: YD; Bølling-Allerød interstadial: BA; Heinrich events (HE1-HE5, blue vertical bars); Dansgaard-Oeschger cooling phases: DO5-11, displayed as bold numbers above light blue vertical bars). The grey rectangle indicates the period of the condensed section (Figure 2), while the dashed grey areas indicate the periods, before and after the condensed section, when sedimentation rates were very low (<5 cm/kyr). Dashed red lines indicate thresholds for the different proxies, while small black arrows indicate peak values as discussed in the main text. (A) Planktonic $\delta^{18}O$ values (‰ VPDB) for cores MD08-3227 (bold black line) and MD99-2339 (thin grey line). The green and red horizontal bars on top of the curves indicate periods of similar and discrepant values, respectively, between cores MD08-3227 and MD99-2339. (B) Reconstruction of the latitudinal position (°N) of the palaeo-Azores Front (AF) for the last 47 kyr according to Bonfardeci et al. (2018). Orange filling indicates position of AF north of 36°N. (C) Benthonic $\delta^{18}O$ values (‰ VPDB) for cores MD08-3227 (bold black line) and MD99-2339 (thin grey line). (D) Planktonic $\delta^{13}C$ values (‰ VPDB) indicating surface productivity. (E) Benthonic $\delta^{13}C$ values (‰ VPDB) for cores MD08-3227 (bold black line) and MD99-2339 (thin grey line), indicative of the amount of organic matter at the seabed. (F) XRF log(Fe/Ca) record. (G) Mean sortable silt (SS) values (μm). From 40 to 34 ka bp, a five-point average is displayed due to the dense amount of data in this interval. (H) Endmember-analysis based on the sedigraph data (silt fraction). Both the aeolian (percentage of EM1+EM2, black line; yellow filling indicates high dust supply) and wind strength proxies (EM1/EM2-ratio, dashed black line) are displayed. (I) Calculated sedimentation rates (SR).

4 | RESULTS

4.1 | Age model and sedimentation rates

The age model of core MD08-3227 (focussing on the upper 1,800 cm of the core) indicates ages ranging between 47 and 0.8 ka BP, thus covering a large part of MIS 3 to the Late Holocene (Figure 3). The age model indicates a large, condensed section, which encompasses the period between *ca* 33 and 19 ka BP. In this condensed section, sedimentation rates are very low, on average 5 cm/kyr, leading to the low resolution of XRF, grain size and isotopic data due to the scarcity of data points (Figure 5).

The sedimentation rates (Figures 2 and 5I), obtained by matching the duration (obtained from the age model) and the sediment thickness, range from 25 to 180 cm/kyr during most of MIS 3 and are maximal during Dansgaard-Oeschger (DO)10 and between Heinrich Event (HE)4 and DO7. At the end of MIS 3 and during the first half of MIS 2, sedimentation rates decrease drastically to below 5 cm/kyr. During the second half of MIS2, rates rise again to 19 cm/kyr and reach a maximum of 90 cm/kyr during the Bølling–Allerød (B–A) interstadial and the onset of the Younger Dryas (YD). During the Holocene, the sedimentation rates are stable at 19 cm/kyr.

4.2 | Isotopic values

The stable isotope data obtained for core MD08-3227 are described and discussed in comparison to data obtained from the nearby located (95 km, Figure 1A) and well-studied core MD99-2339 (Voelker et al., 2006; Waelbroeck et al., 2019). This core, retrieved from 1,170 m water depth, unravelled the regional temporal evolution of the MOW and NACW. For both cores, the same foraminifera species (planktonic: *G. bulloides*, benthonic: *C. pachyderma*) were used for isotopic measurements (Voelker et al., 2006). This allowed the similarities and differences between core MD99-2339, located in a verified MOW setting, and core MD08-3227 (Figure 1) to be compared and contrasted.

For the entire considered period, the planktonic $\delta^{18}O$ values of both records are in approximate agreement (Figure 5A). From 40 to 35 ka BP, the values closely match, as do those for the period between 16 and 14.2 ka BP. From 47 to 40 ka BP, 35 to 33.5 ka BP and 18 to 16 ka BP, the $\delta^{18}O$ values are about 0.5–0.75‰ lower, except for a peak value at 42 ka BP (similar values). A large offset is noticed at the onset of the Holocene (11 ka BP), but this is probably due to the limited data in this interval for core MD99-2339. Holocene $\delta^{18}O$ values in core MD08-3227 are usually about 0.25‰ lower compared to the reference core. The highest $\delta^{18}O$ values (exceeding 1.5‰) are noticed during HE1, but also during DO7, HE4, DO10 and during HE5.

The benthonic $\delta^{18}O$ values (Figure 5C) mostly have an offset of about −1‰ compared to core MD99-2339, except for the period between 46 and 40 ka BP, when the difference gradually diminishes from about −1.5‰ to −1‰. From the Holocene onwards, values decrease constantly, kick-started by a sharp decrease at the end of the YD (Figure 5C). Two intervals of high values (+3‰) stand out: at the onset of HE4 and a longer period lasting from the condensed section to the start of HE1. Also during the YD, the values were higher compared to the surrounding values. Only the low values at the end of HE4 are also seen in core MD99-2339.

The planktonic $\delta^{13}C$ values of core MD08-3227 range between −2.5‰ and 0‰ (Figure 5D). Six peaks are present within the record, all having values above −0.6‰. The peaks occur during the three recorded HE's, as well as during DO10, DO7 and the YD (Figure 5D). The lowest values (below −2‰) are observed between HE4 and DO7, during the B-A interstadial and immediately after the YD.

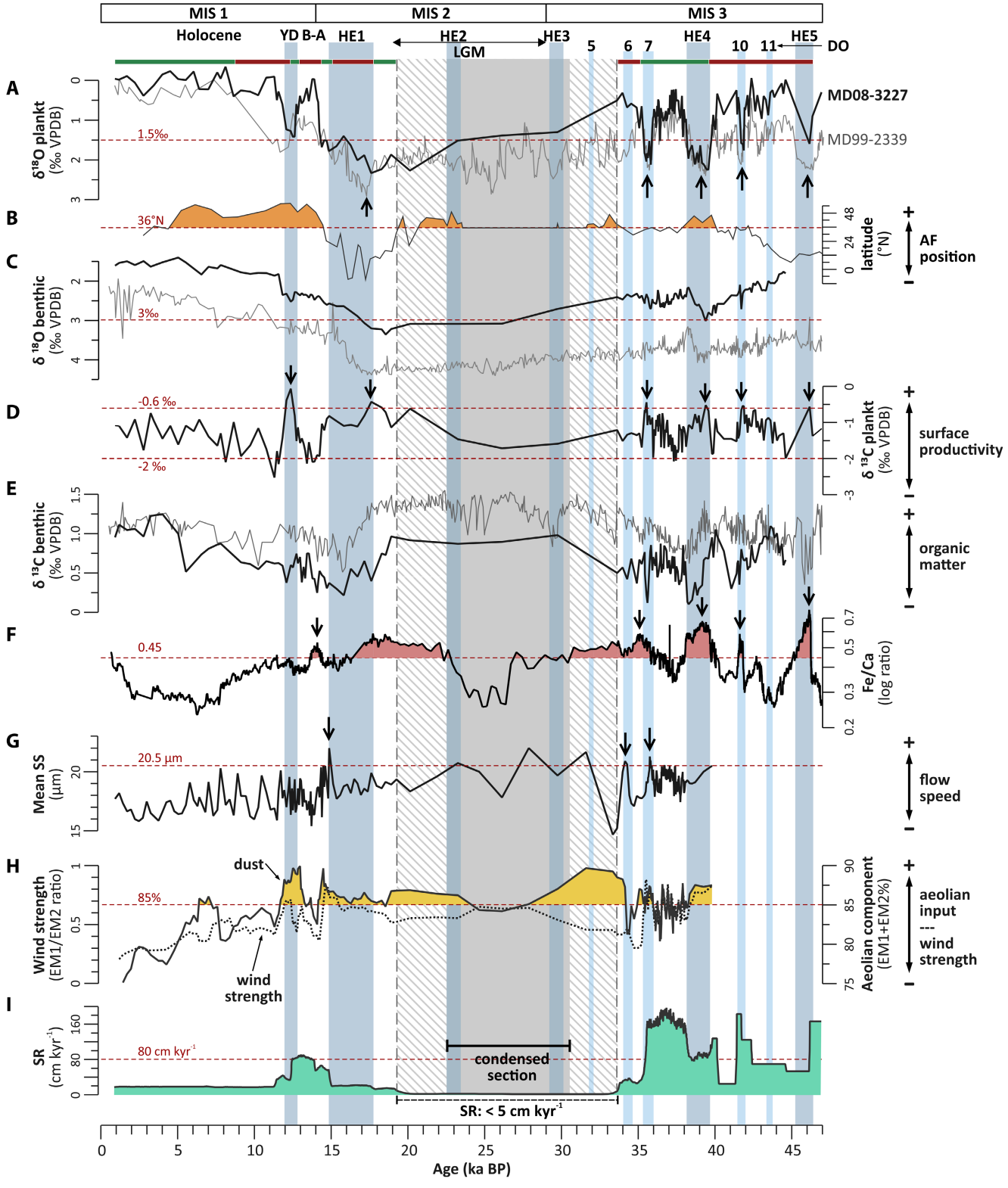

The benthonic $\delta^{13}C$ values of MD08-3227 and MD99-2339 mostly display the same trend (Figure 5E), except for the periods between 46 and 41 ka BP and between 36 and 33 ka BP, when they are in antiphase. From 41 to 36 ka BP, they covary with an offset ranging between −0.5‰ and 0‰, while from 19 ka BP to the end of the YD, the values are in phase with an offset of about 0.35‰ (Figure 5E). During the Holocene, both curves show a slight increasing trend, with values gradually converging, then merging at 5 ka BP.

4.3 | XRF AND GRAIN-SIZE DISTRIBUTION

The XRF log(Fe/Ca) curve (Figure 5F) displays several prominent peaks (high Fe) corresponding to HE5, DO10, HE4, 36–30 ka BP and to the onset of the B–A. Together with the interval between 23 and 17 ka BP, partially coinciding with the last glacial maximum, the log ratio exceeds 0.45 during these periods. The log(Fe/Ca) ratio during MIS 3 is quite different compared to MIS 2. During MIS 3, rapid changes (sometimes exceeding 0.2/100 years) are indicated by small and high peaks, while during MIS 2 and the Holocene, changes are less pronounced and more gradual. At the end of the Holocene, ratios again rise relatively fast (of about 0.15 in 2 kyr).

The mean sortable-silt fraction varies between 15 and 23 μm (Figure 5G). In general, MIS 3 and 2 are characterised by relatively high sortable-silt values (on average 19 μm), although troughs are present in the curve. Prominent peaks are present during DO7 and DO6 and at the end of HE1 (all exceeding 20.5 μm). During the Holocene, an overall decreasing trend is observed (towards 17 μm) with 13 peaks and troughs (between 21 and 16 μm). They occur roughly every 1,000 years.

From the endmember model, three endmembers are retained to ensure comparability with the results of Wienberg et al. (2010). The squared correlation coefficients of the explained variance (r^2) (Prins et al., 1999) with these three endmembers is 0.66. Two endmembers are unimodal (EM3, 2.7 μm and EM2, 8.5 μm), while EM1 reaches a plateau between 15 and 30 μm (supplementary information). Since mean modal grain sizes of present-day aeolian dust, collected along the North West African coast between 33°N and 12°S, vary between 8 and 42 μm (Stuut et al., 2005), EM1 and EM2 are considered of aeolian origin, while EM3 is considered as fluvial material (Wienberg et al., 2010), resulting from hemipelagic transport (Prins et al., 2000). According to Wienberg et al. (2010), EM1/EM2 may be considered to be a measure of relative wind intensity, while aeolian input can be derived from the percentage of EM1+EM2.

Aeolian input is higher between DO6 and DO5, at the beginning of the B-A and during the YD (Figure 5H). A less high, yet distinctive, peak in aeolian input occurs between 8 and 6 ka BP. Periods characterised by sustained high wind strengths occur during DO7, the beginning of the B–A and the YD. Additional smaller increases are noticed in the period between HE4 and DO7 (Figure 5H).

The bulk grain-size analyses over the condensed section are presented in Figure 2. Above 538 cm and below 562 cm, unimodal data (mode of about 10–20 μm) are obtained, while between 562 and 538 cm, bimodal data are present. The modes of the latter are at approximately 20 and 300 μm, with varying proportions of each mode within the section. Higher abundances of the sand fraction (between 540 and 550 cm) are accompanied by the lowest log(Fe/Ca) ratios.

4.4 | Power spectrum

The sortable silt record suggests one cycle meeting the 95% significance level of 1.47 kyr, while planktonic $\delta^{18}O$ values contain three cycles surpassing the 95% confidence level: 9.62, 5.04 and 3.20 kyr. The first two cycles do not meet the threshold of at least four possible cycles within the timeframe of the dataset, yielding only a 3.20 kyr cycle for planktonic $\delta^{18}O$ values (Figure 4).

5 | DISCUSSION

5.1 | A 7.8 kyr condensed section

Based on the sedimentation rates (Figure 5I), a condensed section lasting for 14 kyr (with sedimentation rates as low as 5 cm/kyr) has been identified over the period between 33.5 ka and 19 ka BP, corresponding to a core depth interval of 570 to 527 cm (Figure 3). Contrastingly, the bulk grain size analysis and core image reveal a different story (Figure 2). Sandy sediments, revealed by the bimodal bulk grain size data, are only dominant between 562 and 538 cm. Also, a clear colour boundary in the core image occurs at 538 cm. Both indicate that the end of the condensed section should be set at 538 cm, rather than 527 cm, corresponding to 22.7 ka BP (Figure 2). Similarly, the onset of the condensed section is set at 562 cm, corresponding to 30.5 ka BP, when bimodal grain size assemblages start (Figure 2). Consequently, the condensed section is inferred to last only from 30.5 ka to 22.7 ka BP (Figures 2, 3 and 5). The discrepancy between the extent of the condensed section might be explained by the rather high 2σ error of the age model within the interval 33 to 20 ka BP

(up to 5 kyr; Figure 2), resulting in an overestimation of the duration based on sedimentation rates only.

The inferred 7.8 kyr condensed section is represented by a 24 cm thick interval of foraminifer-rich fine sand (visual core description onboard the RV Marion Dufresne; Van Rooij et al., 2008), comparable to a 'poorly sorted biogenic sandy contouritic sequence' in the classification of Stow and Faugères (2008). The presence of the foraminifer-rich sand layer contrasts with the described overall silty-mud contouritic deposits of this core (Van Rooij et al., 2008). In a silty-muddy environment, the theoretical threshold bottom current velocities should reach to have an erosional effect, at least periodically, is *ca* 50 cm/s (Kuijpers & Nielsen, 2016; Stow et al., 2009). Since visible erosional features, for example sharp boundaries accompanied by large grain-size variations or incisions into underlying sediment, are not associated with the condensed section (Figure 2), bottom current velocities during these 7.8 kyr must have reached speeds close to the boundary erosion/non-deposition, but not exceeded them.

At present, such velocities are reached periodically; tidally modulated bottom current velocities within the NACW/AAIW domain reach maximum speeds of about 45 cm/s (Mienis et al., 2012). Also during the period, the condensed section was created, such strong bottom currents may have persisted. Indeed, Pahnke and Zahn (2005) and Jung et al. (2011) reported increased AAIW production/advection and reduced ocean-atmosphere heat fluxes through heat storage at intermediate (AAIW) water depths during the late MIS 3 (roughly from 35 ka BP towards the Last Glacial Maximum). Moreover, within the southern Gulf of Cádiz, Dubois-Dauphin et al. (2016) documented increased AAIW advection, respectively at 19, *ca* 23.5 and *ca* 27 ka BP, the latter two coinciding with the time frame of the condensed section. The increased advection of AAIW may have resulted in stronger bottom currents for prolonged periods of time within the research area, explaining the near-erosive conditions in the studied drift and allowing the formation of the condensed section.

Besides the long-lasting bottom currents, the occurrence of internal tides at the interface of AAIW and NACW, currently coincident with the core position (642 m water depth), may also have played a crucial role. Nowadays, internal tides are present at this interface (Martins & Vitorino, 2012; Mienis et al., 2012) and it has been inferred that they contribute to the sediment drift build-up within the region (Vandorpe et al., 2016). During DO stadials and HE's, the diminution of sea-surface heat and salinity fluxes towards the north Atlantic (reduced Atlantic meridional circulation) is thought to have caused the accumulation of salt within the mid-depth sub-tropical gyre (Chapman & Maslin, 1999; Voelker et al., 2006). This suggests the existence of a more saline NACW, whereas AAIW is typically characterised by salinity minima (Louarn & Morin, 2011; Machín & Pelegrí, 2009). A more saline NACW and enhanced advection of low-salinity AAIW might have led to a more prominent density gradient, potentially affecting the regional internal tide regime towards more energetic conditions during stadials and consequently led to the formation of the condensed section.

Additionally, the 7.8 kyr condensed section fully coincides with a phase of pronounced CWC growth and mound formation (with aggradation rates of up to 110 cm/kyr) within the Atlantic Moroccan coral province, which lasted roughly from 36 until 19 ka BP (Figure 6; Frank et al., 2011; Hemsing, 2017; Wienberg et al., 2009, 2010). The CWCs are known to exhibit a strong affinity for energetic hydrodynamic conditions, ensuring a substantial food supply (Davies & Guinotte, 2011; Davies et al., 2008; De Clippele et al., 2018; Hebbeln et al., 2016; Thiem et al., 2006). Consequently, the sustained CWC growth during this period further hints towards higher bottom currents.

Within the condensed section, higher percentages of coarse-grained particles are accompanied by much lower ratios of log(Fe/Ca) (Figures 2 and 5F). Assuming the carbonate content mainly consists of biogenic material, this ratio primarily represents the terrigenous versus biogenic fraction (Weltje & Tjallingii, 2008). Given the rather small grain sizes (between 8 and 42 μm) of terrigenous material in the region (Stuut et al., 2005) and the strong bottom currents, only coarser, Ca-rich material remains within the condensed section and consequently decreases the log(Fe/Ca) ratio.

5.2 | Climate variability

5.2.1 | Pre-condensed section: MIS3

High planktonic $\delta^{18}O$ values (exceeding 1.5‰) were obtained during four episodes of MIS3, all of them cold intervals (Figure 5A). These are HE5 (although constrained by just one value), DO10, HE4 and DO7. Except for HE5, these periods agree, both in timing and $\delta^{18}O$ values, with the record from the northern Gulf of Cádiz (MD99-2339; Figure 5A; Toucanne et al., 2007; Voelker et al., 2006).

Combining the planktonic $\delta^{18}O$ values with the Bonfardeci et al. (2018) reconstruction of the position of the palaeo-Azores Front (palaeo-AF; Figure 5B) indicates that during periods when the AF moved far enough north (roughly north of 36°N), similar planktonic $\delta^{18}O$ values in the northern and southern Gulf of Cádiz are obtained and vice versa for southern positions of the front (Figure 5A,B). When the AF is in a southern position, the front has the possibility of entering the Gulf of Cádiz, as is the present situation (Rogerson et al., 2004). This can

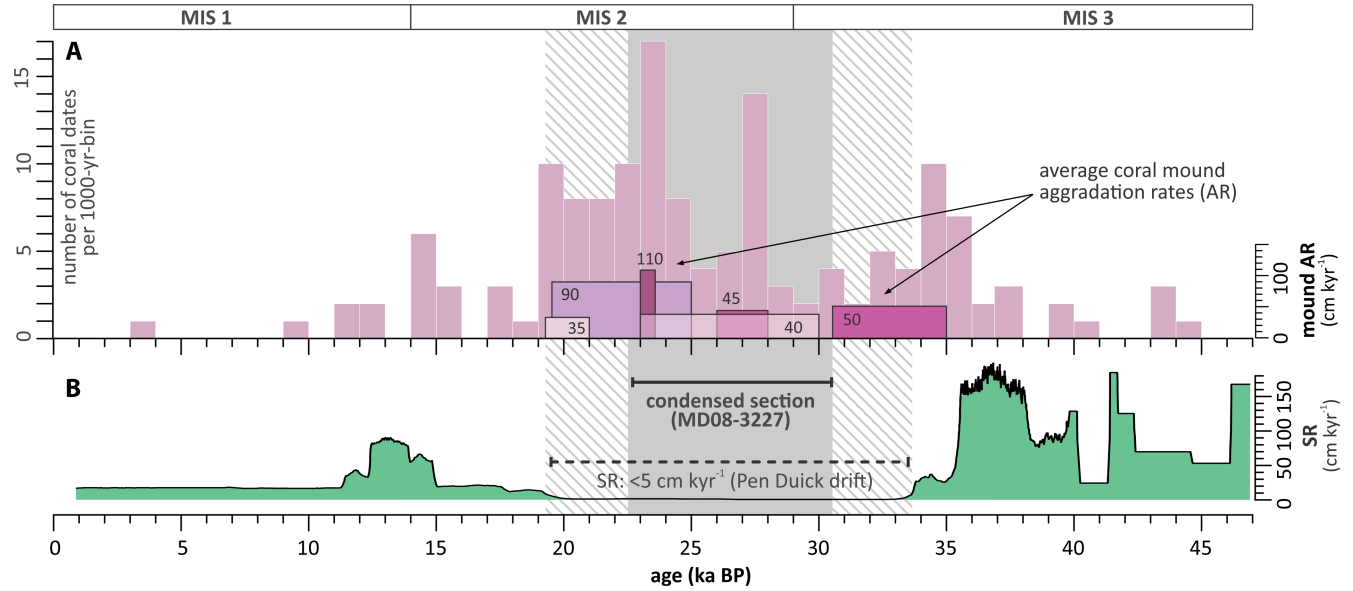

FIGURE 6 (A) Number of dated cold-water corals (pale rose vertical bars, given as 1000-years-bins) obtained from various coral mounds of the southern Gulf of Cádiz (data source: Frank et al., 2011; Hemsing, 2017; Wienberg et al., 2009). The temporal distribution of dated corals during the last 47 kyr is overlain by average coral mound aggradation rates (AR) of >30 cm/kyr (boxes of different pink colours; numbers in or on top the boxes indicate the ARs), which were calculated for individual coral mounds. (B) Sedimentation rate (SR) of core MD08-3227 recovered from the Pen Duick drift. The highest number of dated corals and highest mound ARs correlate well with very low SRs (<5 cm/kyr; dashed grey bar) and the condensed section (grey bar) identified for the drift core.

introduce a sea surface gradient between the northern and southern Gulf of Cádiz, resulting in the discrepant planktonic $\delta^{18}O$ values (Penaud et al., 2011). The results of this study confirm the inferred causal link between the position of the AF and planktonic $\delta^{18}O$ values (Figure 5A,B). Only for the period 35 to 30 ka BP and during DO10, deviating values, not matching with the position of the AF are obtained. This may be due to the lower resolution of both the planktonic $\delta^{18}O$ values (35 to 30 ka BP) and the record from Bonfardeci et al. (2018) or due to a local temperature gradient, lowering the planktonic $\delta^{18}O$ values in the southern Gulf of Cádiz. Similar conclusions regarding the position of the AF in the region have been obtained by former studies (Lebreiro et al., 2018; Voelker et al., 2006).

The planktonic $\delta^{18}O$ values of MIS3 show a 3.2 kyr cyclicity (Figure 4), which is the average spacing of DO and HE events (Figure 5). Dansgaard-Oeschger stadial cycles of 3 and 4.5 kyr, besides the well-known 1.5 kyr cycles, have been reported (Alley et al., 2001; Rahmstorf, 2006), indicating that the planktonic $\delta^{18}O$ values are mainly influenced by northern hemisphere glaciations.

Marine Isotope Stage 3 is characterised by a pronounced cyclicity in the log(Fe/Ca) ratio, matching the $\delta^{18}O$ values with high log(Fe/Ca) during cold periods (HE5, D010, HE4 and DO7; Figure 5A,F). Besides the high log(Fe/Ca) ratio, HE4 and DO7 are also characterised by relatively high wind speeds and more aeolian input (based on the end-member analysis, Figure 5H), which could indicate that colder periods during MIS3 are characterised by stronger wind erosion, supplying more terrigenous (aeolian) material to the study area, resulting in the higher log(Fe/Ca) ratios. Moreover, these cold periods are characterised by higher values of planktonic $\delta^{13}C$ and lower benthonic $\delta^{13}C$ (Figure 5D,E). The planktonic $\delta^{13}C$ values indicate increased productivity through intense wind-driven upwelling regimes, made possible due to enhanced north-eastern trade winds (Eberwein & Mackensen, 2008; Penaud et al., 2010; Wienberg et al., 2010). The low benthonic $\delta^{13}C$ values, which record ^{12}C enrichment, display an inverse trend to the planktonic signal and are interpreted as enhanced particulate organic matter fluxes, in accordance with enhanced sea surface primary productivity (Eberwein & Mackensen, 2006). These findings are, to a large extent, in accordance with regional productivity patterns recorded off the Portuguese margin and in the Gulf of Cádiz (Eynaud et al., 2009; Incarbona et al., 2010). Additionally, Tjallingii et al. (2008) linked the increased primary productivity off Mauritania during each cold period to a shift of the intertropical convergence zone, resulting in increased north-west African aridity and a stronger wind regime. If the intertropical convergence zone moves north, the Azores high and Azores Front will too. The similar planktonic $\delta^{18}O$ values of cores MD08-3227 and MD99-2339 (Figure 5A) provide additional evidence for this northward move.

Since colder periods are characterised by higher input of terrigenous (of aeolian origin) material, but also by increased

primary productivity (Figure 5D), the high log(Fe/Ca) ratio (Figure 5F) indicates that the increased terrigenous supply outmatches the increased input of Ca through enhanced productivity. During warmer periods, less terrigenous material is supplied, but also upwelling and productivity decrease (Figure 5D). The net result is an increase of the ratio of biogenic material and a decreasing log(Fe/Ca) ratio.

5.2.2 | Post-condensed section: MIS 2 and MIS 1

The condensed section ends at 22.7 ka BP, roughly at the end of HE2. Between HE2 and HE1, the AF is mostly situated north of 36°N, resulting in similar planktonic $\delta^{18}O$ values (22.5 to 19 ka BP), while during most of HE1, the AF is situated even south of 30°N (Bonfardeci et al., 2018), yielding the possibility of a Gulf-of-Cádiz-entering branch. This matches with the discrepant planktonic $\delta^{18}O$ values between cores MD08-3227 and MD99-2339 during most of HE1 (Figure 5A) and is confirmed by Rogerson et al. (2004) who reported an eastward branch of the AF penetrating the Gulf of Cádiz prior to 16 ka BP. At the end of HE1 and shortly after it, the eastward branch is absent (Rogerson et al., 2004), explaining the once again similar values.

During the B-A, the position of the AF shifts rapidly northwards (Bonfardeci et al., 2018; Figure 5B), indicating the absence of an eastward branch of the AF. However, the planktonic $\delta^{18}O$ values show a significant offset between cores MD08-3227 and MD99-2339 (Figure 5A), implying a different oceanographic regime in the northern and southern Gulf of Cádiz. Several factors may cause this discrepancy. In the first place, this may have been caused by an eastward branch of the AF, not picked up in the Bonfardeci et al. (2018) data or a temperature gradient of different origin that existed during that period. A second possibility is the incorporation of reworked material containing lower planktonic $\delta^{18}O$ values into the sedimentary sequence, delivered by the bottom currents. Similar transport mechanisms are reported in several studies for the northern Gulf of Cádiz (Alonso et al., 2016; Takashimizu et al., 2016). Despite the lower bottom currents (indicated by the mean sortable silt values) during this period, they may still be able to transport reworked material to the sediment drift. The percentage of EM3 (opposite of the aeolian component, Figure 5H) is markedly higher during the B-A and supports the possibility of fluvial sediment incorporation by the (weaker) bottom currents during this period.

At the start of the YD, the planktonic $\delta^{18}O$ values are similar for cores MD08-3227 and MD99-2339 for about 1 kyr (Figure 5A), while for the remainder of the YD and the start of the Holocene they differ by about 0.5 – 1‰ (Figure 5A). Although Bonfardeci et al. (2018) do indicate a small southward shift of the AF at the start of the YD (Figure 5B), this shift is not sufficient to yield the possibility of an eastward branch of the AF and to explain the dissimilar values for both cores in the Gulf of Cádiz. Unlike Bonfardeci et al. (2018), Rogerson et al. (2004) do report an eastward branch of the AF during this period. The data presented here support the findings of Rogerson et al. (2004) and may imply that a more southward shift than Bonfardeci et al. (2018) indicated took place and lasted longer, from the second half of the YD to the onset of the Holocene.

The largest part of the Holocene is characterised by similar values for cores MD08-3227, MD99-2339 (Figure 5A), MD04-2805CQ (Penaud et al., 2011) and TG2 (Lebreiro et al., 2018), indicating a large displacement of the front, yielding similar conditions (and consequently planktonic $\delta^{18}O$ values) for all four cores. Indeed, Bonfardeci et al. (2018) indicated an extreme northward position (north of 40°N) for most of the Holocene (Figure 5B), rendering an eastward branch entering the Gulf of Cádiz impossible and explaining the similar values for all cores.

The log(Fe/Ca) ratio displays an overall decreasing trend from the end of the Last Glacial Maximum until the end of the Holocene (3 ka BP), after which an increase is noticed again (Figure 5F). One marked increase in log(Fe/Ca) is present during the B–A, coeval with a large decrease in both aeolian input and wind speed (Figure 5H). Given the large decrease in aeolian input (and input of Fe), a relatively larger decrease in biogenic Ca rather than an increase of terrigenous material is inferred for the higher log(Fe/Ca) ratios. This is confirmed by the planktonic $\delta^{13}C$ values, which drop during the B–A (Figure 5D), inferring lower primary productivity and consequently lower rates of biogenic Ca. During the last 19 kyr, the planktonic $\delta^{13}C$ values show two distinct intervals of high values (HE1 and YD; Figure 5D). Similar to MIS3, benthonic $\delta^{13}C$ values during HE1 and the YD display an inverse trend to the planktonic signal (Figure 5D,E), hinting towards enhanced particulate organic matter fluxes during periods of enhanced primary productivity. Similar findings for the Iberian margin have been described by Penaud et al. (2011).

5.3 | Drift build-up: water masses and controls

5.3.1 | Water masses

For sediment drifts in the southern Gulf of Cádiz, two water masses are considered to be of prime importance. While MOW is held responsible for the drift deposits recovered within core TG2 by Lebreiro et al. (2018), Vandorpe et al. (2016) linked the sediment drifts in the

EAMVP to AAIW. Lebreiro et al. (2018) related high values of benthonic $\delta^{13}C$ at site TG2 to higher portions of a southward-flowing upper MOW. Four of these short-lived episodes are recorded in core TG2 and can be linked to periods with deposition of silty contourites. For most of the last 19 ka BP, the benthonic $\delta^{13}C$ values of core MD99-2339 (within the MOW pathway) and MD08-3227 (this study) are in phase (Figure 5E; correlation coefficient of 0.532) and the values for cores TG2 and MD08-3227 are very similar (average difference below 0.2‰), indicating that this southern branch of MOW may have played a role in shaping the Pen Duick drift during this period.

However, the Pen Duick drift is currently influenced by the AAIW/NACW interface, and several authors have suggested that the AAIW was also the predominant influence during the Last Glacial Maximum (Dubois-Dauphin et al., 2016; Mienis et al., 2012; Vandorpe et al., 2014, 2016). Pahnke et al. (2008) recorded periods of increased AAIW influence during the last 20 kyr within the western subtropical Atlantic and Penaud et al. (2010) attested the presence of a hydrological structure during HE2, HE1 and the YD, separating the southern and northern Gulf of Cádiz water masses. This renders the influence of MOW on the Pen Duick drift difficult during these periods and supports AAIW as the most influential water mass. Moreover, benthonic $\delta^{18}O$ values during HE1 decrease gradually by about 0.75‰ for core MD08-3227 (Figure 5C), which are values associated with global sea-level rises (Voelker et al., 2006; Waelbroeck et al., 2019), while for core MD99-2339, values decrease drastically (Figure 5C), indicative of an invigorated MOW (Voelker et al., 2006). If MOW played a role in shaping the Pen Duick drift, one would have expected a decrease of the same magnitude as in the northern Gulf of Cádiz. These contrasting differences indicate that MOW probably played a very limited role in shaping the Pen Duick drift during HE1, the YD and most likely during the entire post-condensed section period. Since core TG2 is located about 50 km south of core MD08-3227, MOW-influence at that location cannot be excluded based on this papers findings.

During MIS3, the correlation coefficient of benthonic $\delta^{13}C$ values of cores MD08-3227 and MD99-2339 (MOW-shaped location) is −0.182, indicating that MOW most likely also played no defining role in shaping the EAMVP sediment drifts before the condensed section. Within the sub-tropical Atlantic, AAIW productivity increases during DO stadials and is coeval with periods of reduced Atlantic meridional circulation (Anderson et al., 2009; Henry et al., 2016; Jung et al., 2011; Skinner et al., 2010). The increased productivity during DO stadials (Figure 5D) results in enhanced advection of AAIW, which provides a suitable mechanism to explain the bottom current variability prior to 30.5 ka BP, which is markedly higher during DO6, DO7 and HE4 (higher mean sortable silt values, Figure 5G). In addition, the sortable silt data contain a 1.47 kyr cyclicity during MIS 3 (Figure 4), which is the spacing of DO events (Alley et al., 2001). This is characteristic for the north-east Atlantic, where millennial-scale DO stadial/interstadial cycles span from 33 to 50 ka BP (Hodell et al., 2013; Martrat et al., 2007; Shackleton et al., 2000; Voelker et al., 2006). The matching cyclicity and higher bottom currents during DO events both hint towards AAIW influence during MIS3 in the studied area.

5.3.2 | Bottom current variability and sediment supply

Sediment drifts are typically associated with increased sedimentation rates (Rebesco et al., 2014) and are ubiquitous in the area (Vandorpe et al., 2016). They result from enhanced bottom currents, for which sortable silt is known to be a good indicator (McCave, 2008; McCave & Hall, 2006; McCave et al., 1995, 2017). The variations in sortable silt of core MD08-3227 (Figure 5G) may indeed result from winnowing of the fine terrigenous fraction within sediment drifts due to enhanced bottom currents (Alonso et al., 2016; Gonthier et al., 1984; McCave et al., 1995; Nelson et al., 1993; Stow et al., 2002). However, the increases in (sortable) silt in the area have previously often been interpreted as increased aeolian dust input associated with north-west African aridification periods (Holz et al., 2007; Rodrigo-Gámiz et al., 2014).

Differentiating between both explanations is not straightforward. For example, Vandorpe et al. (2014) indicated variations in drift growth on larger time scale within the Pen Duick drift (100 kyr periods), related to changing bottom current velocities, while Wienberg et al. (2010) considered the main coarse sediment source (i.e. >6 μm), and hence (sortable) silt variations, to be predominantly of aeolian dust origin. The latter interpretation agrees with enhanced aeolian dust input during DO stadials off Mauritania (Tjallingii et al., 2008) and may additionally provide a suitable driving mechanism to explain the productivity pattern, reflected in the planktonic $\delta^{13}C$ values (Figure 5D). Such findings are also reported by Penaud et al. (2010) and Wienberg et al. (2010). However, they do not exclude the possible (additional) influence of bottom currents. Comparing the sedimentation rates of cores MD08-3227 and GeoB9064 (Wienberg et al., 2010), situated only 25 km north of MD08-3227, shows that rates up to *ca* 25 cm/kyr are reported for GeoB9064, while rates exceeding

50 cm/kyr are regularly observed for core MD08-3227, with peaks even exceeding 100 cm/kyr. If the entire region is affected solely by changes in aeolian dust input, equal sedimentation rates would be expected for sites so close to each other. Given the much higher rates for core MD08-3227, the influence of bottom currents is likely, which can affect the sortable silt variations of core MD08-3227 as well.

Finding out which factor (aeolian input or bottom currents) is the most important at each stage is difficult, although the dataset does give some indications. From HE4 to DO7, overall high values of mean sortable silt (around 20 μm) are noticed, matched by the highest sedimentation rates obtained for the last 47 kyr (up to 200 cm/kyr; Figure 5G,I). During this period, aeolian input is variable, but not synchronous with the sedimentation rates (correlation coefficient of −0.190; Figure 5H). This indicates that the high sedimentation rates are most likely related to drift development and higher bottom currents and to a lesser extent to variations in aeolian input. Also during DO6, a peak in sortable silt is matched by a minimum in aeolian input and slightly higher sedimentation rates (compared to the surrounding values, Figure 5G,H,I). The higher sortable silt values during DO6 might again be due to drift build-up and elevated bottom currents.

During the last 23 kyr, the picture is different. Sedimentation rates exceeding 50 cm/kyr are only observed during the B–A and the YD (Figure 5I), periods matched by two distinct peaks in aeolian input, together covering a substantial part of this period (Figure 5H). Consequently, one could conclude that the higher sedimentation rates (and consequently drift build-up) are most likely related to increased aeolian input. However, since the nearby site GeoB9064 displays much lower sedimentation rates during this period (*ca* 25 cm/kyr), bottom currents are believed to play a role as well and can explain these much higher sedimentation rates. Consequently, drift build-up during the post-condensed section is coeval with enhanced aeolian input, but bottom currents have an amplifying effect on the sedimentation rates. Considering the last 47 kyr, the build-up of the Pen Duick drift seems to be mainly controlled by elevated bottom currents, but after the condensed section, aeolian input also plays an important role.

6 | CONCLUSIONS

The study of the 47 kyr long sedimentary record of the Pen Duick drift along the Moroccan Atlantic margin provides detailed insights on the palaeoceanography of the region, but also sheds insights into the regional palaeoclimatology. The main findings are summarised below.

1. A 7.8 kyr condensed section is present within the sedimentary record of the Pen Duick drift, characterised by low sedimentation rates and low log(Fe/Ca) ratios. The condensed section is the result of enhanced long-lasting bottom currents and increased internal tidal energy due to higher density differences between two overlying water masses, in this case (glacial) NACW and AAIW.
2. The formation of the condensed section occurred contemporaneous to a prolific cold-water coral growth phase in the southern Gulf of Cádiz. During this period, enhanced bottom currents are inferred, preventing the deposition of sediment within the sediment drift. Consequently, sediments remained longer in suspension, allowing them to be baffled by the corals and depositing them in their framework. This showcases the need for studying both on-mound and off-mound cores (Hebbeln et al., 2019b) when investigating the formation of a cold-water coral mound province across climate cycles.
3. The presence of the AAIW-shaped Pen Duick drift renders it the most distal sedimentary expression of AAIW within the entire North-East Atlantic. This highlights once more how sedimentation patterns can still be affected by a water mass, even though they are located so far from the source region of the responsible water mass.
4. The sedimentation rates within the Pen Duick drift are not only influenced by the action of the bottom currents, but also by the input of (aeolian) sediment. Increased aeolian input during mainly colder periods, provided more input for the Pen Duick drift, allowing it to reach sedimentation rates exceeding 80 cm/kyr at times.
5. Palaeoclimate conditions in the southern Gulf of Cádiz seem to be mainly controlled by the position of the Azores Front (AF). When the AF shifted far enough north (north of 36°N), similar climate conditions are inferred for the northern and southern Gulf of Cádiz, while southward shifts induced a Gulf of Cádiz-penetrating branch of the AF, resulting in different conditions north and south of this branch.
6. Although MOW is inferred to be present 50 km south of the Pen Duick Escarpment (Lebreiro et al., 2018), the Pen Duick drift is mainly built up under the action of the (glacial) AAIW and the overlying NACW. Consequently, this study confirms the AAIW as the main drift-building water mass within the southern Gulf of Cádiz. However, questions are being raised regarding the temporal and spatial variability of both

MOW and AAIW within the southern Gulf of Cádiz. How far north does the AAIW reach? What is the temporal and spatial impact of both water masses on the sedimentation patterns in the southern Gulf of Cádiz? How, where and when did these water masses interact? These questions can only be solved by strategically sampling additional (drift) systems in the southern Gulf of Cádiz and investigating the palaeoceanographic and palaeoclimate evolution of these cores.

ACKNOWLEDGEMENTS

This study was carried out within the framework of a Ghent University BOF 'Starting Grant'. It was additionally part of the FWO project Contourite-3D (n° 1524713N). The authors wish to acknowledge the captains and crews of the campaigns on board of the R/V Marion Dufresne cruise MD169-MICROSYSTEMS (founded by European Science Foundation, EuroDIVERSITY within the framework of project EC FP6 IP HERMES) and of the R/V Belgica cruise 2013/16-COMIC. Shiptime on board R/V Belgica was provided by BELSPO and RBINS–OD Nature. Stable isotopes analyses were performed on Panoply Platerform Mass spectrometer at LSCE. A special thanks to Gulay Isguder who helped us in the foraminifera determination and to Alice Matossian and Lotte Verweirder for providing additional bulk grain sizes on the condensed section. This study contributes to the Deutsche Forschungsgemeinschaft DFG-project 'MoccaMeBo' (He3412-18). Two anonymous reviewers helped a lot in improving the content of the manuscript.

DATA AVAILABILITY STATEMENT

Data sharing is not applicable to this article as no new data were created or analysed in this study.

ORCID

Thomas Vandorpe https://orcid.org/0000-0002-1461-2484
Claudia Wienberg https://orcid.org/0000-0001-9870-5495

REFERENCES

Alley, R.B., Anandakrishnan, S. & Jung, P. (2001) Stochastic resonance in the North Atlantic. *Paleoceanography*, *16*, 190–198.

Alonso, B., Ercilla, G., Casas, D., Stow, D.A.V., Rodríguez-Tovar, F.J., Dorador, J. & Hernández-Molina, F.-J. (2016) Contourite vs gravity-flow deposits of the Pleistocene Faro Drift (Gulf of Cadiz): Sedimentological and mineralogical approaches. *Marine Geology*, *377*, 77–94.

Alonso, B., Juan, C., Ercilla, G., Cacho, I., López-González, N., Rodríquez-Tovar, F.J., Dorador, J., Francés, G., Casas, D., Vandorpe, T. & Vázquez, J.T. (2021) Paleoceanographic and paleoclimatic variability in the Western Mediterranean during the last 25 cal. kyr BP. New insights from contourite drifts. *Marine Geology*, *437*, 106488.

Alves, M., Gaillard, F., Sparrow, M., Knoll, M. & Giraud, S. (2002) Circulation patterns and transport of the Azores Front-Current system. *Deep Sea Research Part II: Topical Studies in Oceanography*, *49*, 3983–4002.

Ambar, I., Serra, N., Neves, F. & Ferreira, T. (2008) Observations of the Mediterranean Undercurrent and eddies in the Gulf of Cadiz during 2001. *Journal of Marine Systems*, *71*, 195–220.

Anderson, R.F., Ali, S., Bradtmiller, L.I., Nielsen, S.H.H., Fleisher, M.Q., Anderson, B.E. & Burckle, L.H. (2009) Wind-driven upwelling in the southern ocean and the deglacial rise in atmospheric CO_2. *Science*, *323*, 1443–1448.

Böhm, E., Lippold, J., Gutjahr, M., Frank, M., Blaser, P., Antz, B., Fohlmeister, J., Frank, N., Andersen, M.B. & Deininger, M. (2015) Strong and deep Atlantic meridional overturning circulation during the last glacial cycle. *Nature*, *517*, 73–76.

Bonfardeci, A., Caruso, A., Bartolini, A., Bassinot, F. & Blanc-Valleron, M.-M. (2018) Distribution and ecology of the Globigerinoides ruber — Globigerinoides elongatus morphotypes in the Azores region during the late Pleistocene-Holocene. *Palaeogeography, Palaeoclimatology, Palaeoecology*, *491*, 92–111.

Brackenridge, R., Stow, D., Hernández-Molina, F., Jones, C., Mena, A., Alejo, I., Ducassou, E., Llave, E., Ercilla, G., Nombela, M., Pérez-Arlucea, M. & Francés, G. (2018) Textural characteristics and facies of sand-rich contourite depositional systems. *Sedimentology*, *65*, 2232–2252.

Cabecadas, G., José Brogueira, M. & Goncalves, C. (2002) The chemistry of Mediterranean outflow and its interactions with surrounding waters. *Deep Sea Research Part II: Topical Studies in Oceanography*, *49*, 4263–4270.

Cacho, I., Grimalt, J.O., Sierro, F.J., Shackleton, N. & Canals, M. (2000) Evidence for enhanced Mediterranean thermohaline circulation during rapid climatic coolings. *Earth and Planetary Science Letters*, *183*, 417–429.

Carracedo Segade, L.I., Gilcoto, M., Mercier, H. & Pérez, F.F. (2015) Quasi-synoptic transport, budgets and water mass transformation in the Azores–Gibraltar Strait region during summer 2009. *Progress in Oceanography*, *130*, 47–64.

Chapman, M.R. & Maslin, M.A. (1999) Low-latitude forcing of meridional temperature and salinity gradients in the subpolar North Atlantic and the growth of glacial ice sheets. *Geology*, *27*, 875–878.

Chen, H., Xie, X., Van Rooij, D., Vandorpe, T., Su, M. & Wang, D. (2014) Depositional characteristics and processes of alongslope currents related to a seamount on the northwestern margin of the Northwest Sub-Basin, South China Sea. *Marine Geology*, *355*, 36–53.

Chen, H., Xie, X., Zhang, W., Shu, Y., Wang, D., Vandorpe, T. & Van Rooij, D. (2016) Deep-water sedimentary systems and their relationship with bottom currents at the intersection of Xisha Trough and Northwest Sub-Basin, South China Sea. *Marine Geology*, *378*, 101–113.

Coplen, T.B. (1996) New guidelines for reporting stable hydrogen, carbon, and oxygen isotope-ratio data. *Geochimica et Cosmochimica Acta*, *60*, 3359–3360.

Cropper, T.E., Hanna, E. & Bigg, G.R. (2014) Spatial and temporal seasonal trends in coastal upwelling off Northwest Africa, 1981–2012. *Deep Sea Research Part I: Oceanographic Research Papers*, *86*, 94–111.

Davies, A.J. & Guinotte, J.M. (2011) Global habitat suitability for framework-forming cold-water corals. *PLoS ONE*, *6*, e18483.

Davies, A.J., Wisshak, M., Orr, J.C. & Roberts, M.J. (2008) Predicting suitable habitat for the cold-water coral Lophelia pertusa (Scleractinia). *Deep Sea Research Part I: Oceanographic Research Papers*, *55*, 1048–1062.

De Clippele, L.H., Huvenne, V.A.I., Orejas, C., Lundälv, T., Fox, A., Hennige, S.J. & Roberts, J.M. (2018) The effect of local hydrodynamics on the spatial extent and morphology of cold-water coral habitats at Tisler Reef, Norway. *Coral Reefs*, *37*, 253–266.

Dietze, E. & Dietze, M. (2019) Grain-size distribution unmixing using the R package EMMAgeo. *E&G Quaternary Science Journal*, *68*, 29–46.

Dubois-Dauphin, Q., Bonneau, L., Colin, C., Montero-Serrano, J.-C., Montagna, P., Blamart, D., Hebbeln, D., Van Rooij, D., Pons-Branchu, E., Hemsing, F., Wefing, A.-M. & Frank, N. (2016) South Atlantic intermediate water advances into the North-east Atlantic with reduced Atlantic meridional overturning circulation during the last glacial period. *Geochemistry, Geophysics, Geosystems*, *17*, 2336–2353.

Eberwein, A. & Mackensen, A. (2006) Regional primary productivity differences off Morocco (NW-Africa) recorded by modern benthic foraminifera and their stable carbon isotopic composition. *Deep Sea Research Part I: Oceanographic Research Papers*, *53*, 1379–1405.

Eberwein, A. & Mackensen, A. (2008) Last glacial maximum paleoproductivity and water masses off NW-Africa: Evidence from benthic foraminifera and stable isotopes. *Marine Micropaleontology*, *67*, 87–103.

Eynaud, F., De Abreu, L., Voelker, A., Schönfeld, J., Salgueiro, E., Turon, J.-L., Penaud, A., Toucanne, S., Naughton, F., Sánchez Goñi, M.F., Malaizé, B. & Cacho, I. (2009) Position of the Polar Front along the western Iberian margin during key cold episodes of the last 45 ka. *Geochemistry, Geophysics, Geosystems*, *10*.

Faugères, J.C. & Stow, D.A.V. (2008) Contourite drifts: Nature, Evolution and Controls. In: Rebesco, M. & Camerlenghi, A. (Eds.) *Contourites*. Amsterdam: Elsevier.

Faugères, J.-C., Stow, D.A.V., Imbert, P. & Viana, A. (1999) Seismic features diagnostic of contourite drifts. *Marine Geology*, *162*, 1–38.

Flinch, J. F. (1993) Tectonic evolution of the Gibraltar Arc. PhD, Rice University.

Foubert, A., Depreiter, D., Beck, T., Maignien, L., Pannemans, B., Frank, N., Blamart, D. & Henriet, J.-P. (2008) Carbonate mounds in a mud volcano province off north-west Morocco: key to processes and controls. *Marine Geology*, *248*, 74–96.

Frank, N., Freiwald, A., Correa, M.L., Wienberg, C., Eisele, M., Hebbeln, D., Van Rooij, D., Henriet, J.-P., Colin, C., Van Weering, T., De Haas, H., Buhl-Mortensen, P., Roberts, J.M., De Mol, B., Douville, E., Blamart, D. & Hatté, C. (2011) Northeastern Atlantic cold-water coral reefs and climate. *Geology*, *39*, 743–746.

Freeman, E., Skinner, L.C., Tisserand, A., Dokken, T., Timmermann, A., Menviel, L. & Friedrich, T. (2015) An Atlantic–Pacific ventilation seesaw across the last deglaciation. *Earth and Planetary Science Letters*, *424*, 237–244.

Gonthier, E.G., Faugères, J.-C. & Stow, D.A.V. (1984) Contourite facies of the Faro Drift, Gulf of Cadiz. *Geological Society London, Special Publications*, *15*, 275–292.

Hanebuth, T.J.J., Zhang, W., Hofmann, A.L., Löwemark, L.A. & Schwenk, T. (2015) Oceanic density fronts steering bottom-current induced sedimentation deduced from a 50 ka contourite-drift record and numerical modeling (off NW Spain). *Quaternary Science Reviews*, *112*, 207–225.

Hebbeln, D., Wienberg, C., Bartels, M., Bergenthal, M., Frank, N., Gaide, S., Henriet, J. P., Kaszemeik, K., Klar, S., Klein, T., Krengel, T., Kuhnert, M., Meyer-Schack, B., Noorlander, C., Reuter, M., Rosiak, U., Schmidt, W., Seeba, H., Seiter, C., Strange, N., Terhzaz, L. & Van Rooij, D. (2015) MoccoMeBo climate-driven development of Moroccan cold-water coral mounds revealed by MeBo-drilling: Atlantic vs. Mediterranean settings—cruise MSM36—February 18–March 14, 2014—Malaga (Spain)—Las Palmas (Spain). MARIA S. MERIAN -berichte, MSM36. DFG-Senatskommission für Ozeanographie.

Hebbeln, D., Van Rooij, D. & Wienberg, C. (2016) Good neighbours shaped by vigorous currents: Cold-water coral mounds and contourites in the North Atlantic. *Marine Geology*, *378*, 171–185.

Hebbeln, D., Bender, M., Gaide, S., Titschack, J., Vandorpe, T., Van Rooij, D., Wintersteller, P. & Wienberg, C. (2019a) Thousands of cold-water coral mounds along the Moroccan Atlantic continental margin: Distribution and morphometry. *Marine Geology*, *411*, 51–61.

Hebbeln, D., Portilho-Ramos, R.D.C., Wienberg, C. & Titschack, J. (2019b) The Fate of Cold-Water Corals in a Changing World: A Geological Perspective. *Frontiers in Marine Science*, *6*.

Heezen, B.C., Hollister, C.D. & Ruddiman, W.F. (1966) Shaping of the continental rise by deep geostrophic currents. *Science*, *152*, 502–508.

Hemsing, F. (2017) Cold-water corals as archives for ocean dynamics, environmental conditions and glacial reef accumulation. Dissertation, Ruperto-Carola-University of Heidelberg.

Henry, L.G., Mcmanus, J.F., Curry, W.B., Roberts, N.L., Piotrowski, A.M. & Keigwin, L.D. (2016) North Atlantic ocean circulation and abrupt climate change during the last glaciation. *Science*, *353*, 470–474.

Hernández-Molina, F.J., Somoza, L., Vazquez, J.T., Lobo, F., Fernández-Puga, M.C., Llave, E. & Díaz-Del Río, V. (2002) Quaternary stratigraphic stacking patterns on the continental shelves of the southern Iberian Peninsula: their relationship with global climate and palaeoceanographic changes. *Quaternary International*, *92*, 5–23.

Hernández-Molina, F.J., Llave, E., Stow, D.A.V., Garciá, M., Somoza, L., Vázquez, J.T., Lobo, F.J., Maestro, A., Díaz Del Río, G., León, R., Medialdea, T. & Gardner, J. (2006) The contourite depositional system of the Gulf of Cádiz: A sedimentary model related to the bottom current activity of the Mediterranean outflow water and its interaction with the continental margin. *Deep Sea Research Part II: Topical Studies in Oceanography*, *53*, 1420–1463.

Hernández-Molina, F.J., Serra, N., Stow, D.A.V., Llave, E., Ercilla, G. & Van Rooij, D. (2011) Along-slope oceanographic processes and sedimentary products around the Iberian margin. *Geo-Marine Letters*, *31*, 315–341.

Hernández-Molina, F.J., Soto, M., Piola, A.R., Tomasini, J., Preu, B., Thompson, P., Badalini, G., Creaser, A., Violante, R.A., Morales, E., Paterlini, M. & De Santa Ana, H. (2016) A contourite depositional system along the Uruguayan continental margin: sedimentary, oceanographic and paleoceanographic implications. *Marine Geology*, *378*, 333–349.

Hodell, D., Crowhurst, S., Skinner, L., Tzedakis, P.C., Margari, V., Channell, J.E.T., Kamenov, G., Maclachlan, S. & Rothwell, G. (2013) Response of Iberian Margin sediments to orbital and

suborbital forcing over the past 420 ka. *Paleoceanography*, *28*, 185–199.

Holz, C., Stuut, J.-B.W., Henrich, R. & Meggers, H. (2007) Variability in terrigenous sedimentation processes off northwest Africa and its relation to climate changes: Inferences from grain-size distributions of a Holocene marine sediment record. *Sedimentary Geology*, *202*, 499–508.

Hoogakker, B.A.A., Chapman, M.R., Mccave, I.N., Hillaire-Marcel, C., Ellison, C.R.W., Hall, I.R. & Telford, R.J. (2011) Dynamics of North Atlantic deep water masses during the Holocene. *Paleoceanography*, *26*, PA4214.

Huang, K.-F., Oppo, D.W. & Curry, W.B. (2014) Decreased influence of Antarctic intermediate water in the tropical Atlantic during North Atlantic cold events. *Earth and Planetary Science Letters*, *389*, 200–208.

Incarbona, A., Martrat, B., Di Stefano, E., Grimalt, J.O., Pelosi, N., Patti, B. & Tranchida, G. (2010) Primary productivity variability on the Atlantic Iberian Margin over the last 70,000 years: Evidence from coccolithophores and fossil organic compounds. *Paleoceanography*, *25*, PA2218.

Iorga, M.C. & Lozier, M.S. (1999) Signatures of the Mediterranean outflow from a North Atlantic climatology: 1. Salinity and density fields. *Journal of Geophysical Research: Oceans*, *104*, 25985–26009.

Jung, S.J.A., Kroon, D., Ganssen, G., Peeters, F. & Ganeshram, R. (2011) Southern Hemisphere intermediate water formation and the bi-polar seesaw. *Pages News*, *18*, 36–38.

Kuijpers, A. & Nielsen, T. (2016) Near-bottom current speed maxima in North Atlantic contourite environments inferred from current-induced bedforms and other seabed evidence. *Marine Geology*, *378*, 230–236.

Lebreiro, S., Anton, L., Reguera, M.I. & Marzocchi, A. (2018) Paleoceanographic and climatic implications of a new Mediterranean Outflow branch in the southern Gulf of Cadiz. *Quaternary Science Reviews*, *197*, 92–111.

Liu, S., Van Rooij, D., Vandorpe, T., González-Pola, C., Ercilla, G. & Hernández-Molina, F.J. (2019) Morphological features and associated bottom-current dynamics in the Le Danois Bank region (southern Bay of Biscay, NE Atlantic): A model in a topographically constrained small basin. *Deep Sea Research Part I: Oceanographic Research Papers*, *149*, 103054.

Llave, E., Schönfeld, J., Hernández-Molina, F.J., Mulder, T., Somoza, L., Díaz Del Río, V. & Sánchez-Almazo, I. (2006) High-resolution stratigraphy of the Mediterranean outflow contourite system in the Gulf of Cadiz during the late Pleistocene: The impact of Heinrich events. *Marine Geology*, *227*, 241–262.

Llave, E., Hernández-Molina, F., Stow, D.V., Fernández-Puga, M., García, M., Vázquez, J., Maestro, A., Somoza, L. & Díaz Del Río, V. (2007a) Reconstructions of the Mediterranean outflow water during the quaternary based on the study of changes in buried mounded drift stacking pattern in the Gulf of Cadiz. *Marine Geophysical Researches*, *28*, 379–394.

Llave, E., Hernández-Molina, F.J., Somoza, L., Stow, D.A.V. & Díaz Del Río, V. (Eds.). (2007b) Quaternary evolution of the contourite depositional system in the Gulf of Cadiz. *Geological Society, London, Special Publications*, *276*, 49–79.

Llave, E., Matias, H., Hernández-Molina, F., Ercilla, G., Stow, D. & Medialdea, T. (2011) Pliocene–Quaternary contourites along the northern Gulf of Cadiz margin: sedimentary stacking pattern and regional distribution. *Geo-Marine Letters*, *31*, 377–390.

Lofi, J., Voelker, A.H.L., Ducassou, E., Hernández-Molina, F.J., Sierro, F.J., Bahr, A., Galvani, A., Lourens, L.J., Pardo-Igúzquiza, E., Pezard, P., Rodríguez-Tovar, F.J. & Williams, T. (2016) Quaternary chronostratigraphic framework and sedimentary processes for the Gulf of Cadiz and Portuguese Contourite Depositional Systems derived from Natural Gamma Ray records. *Marine Geology*, *377*, 40–57.

Lomb, N.R. (1976) Least-squares frequency analysis of unequally spaced data. *Astrophysics and Space Science*, *39*, 447–462.

Louarn, E. & Morin, P. (2011) Antarctic Intermediate Water influence on Mediterranean Sea Water outflow. *Deep Sea Research Part I: Oceanographic Research Papers*, *58*, 932–942.

Lougheed, B.C. & Obrochta, S.P. (2016) MatCal: Open Source Bayesian 14C Age Calibration in Matlab. *Journal of Open Research Software*, *4*, 42.

Lynch-Stieglitz, J., Adkins, J.F., Curry, W.B., Dokken, T., Hall, I.R., Herguera, J.C., Hirschi, J.J.-M., Ivanova, E.V., Kissel, C., Marchal, O., Marchitto, T.M., Mccave, I.N., Mcmanus, J.F., Mulitza, S., Ninnemann, U., Peeters, F., Yu, E.-F. & Zahn, R. (2007) Atlantic meridional overturning circulation during the last glacial maximum. *Science*, *316*, 66–69.

Machín, F. & Pelegrí, J.L. (2009) Northward Penetration of Antarctic Intermediate Water off Northwest Africa. *Journal of Physical Oceanography*, *39*, 512–535.

Machín, F., Pelegrí, J.L., Marrero-Díaz, A., Laiz, I. & Ratsimandresey, A.W. (2006) Near-surface circulation in the southern Gulf of Cádiz. *Deep Sea Research Part II: Topical Studies in Oceanography*, *53*, 1161–1181.

Maldonado, A., Somoza, L. & Pallarés, L. (1999) The Betic orogen and the Iberian-African boundary in the Gulf of Cadiz: geological evolution (central North Atlantic). *Marine Geology*, *155*, 9–43.

Martins, I. & Vitorino, J. (2012) Physical processes affecting the El-Arraiche mud volcano Field (NW Moroccan Margin). HERMIONE Final Meeting, Carvoeiro.

Martrat, B., Grimalt, J.O., Shackleton, N.J., De Abreu, L., Hutterli, M.A. & Stocker, T.F. (2007) Four climate cycles of recurring deep and surface water destabilizations on the Iberian Margin. *Science*, *317*, 502–507.

Mccave, I.N. (2008) Size sorting during transport and deposition of fine sediments: sortable silt and flow speed. *Developments in Sedimentology*, *60*, 379–407.

Mccave, I.N. & Hall, I.R. (2006) Size sorting in marine muds: Processes, pitfalls and prospects for paleoflow-speed proxies. *Geochemistry, Geophysics, Geosystems*, *7*, Q10N05.

Mccave, I.N., Manighetti, B. & Robinson, S.G. (1995) Sortable silt and fine sediment size/composition slicing: Parameters for palaeocurrent speed and palaeoceanography. *Paleoceanography*, *10*, 593–610.

Mccave, I.N., Thornalley, D.J.R. & Hall, I.R. (2017) Relation of sortable silt grain-size to deep-sea current speeds: Calibration of the 'Mud Current Meter'. *Deep Sea Research Part I: Oceanographic Research Papers*, *127*, 1–12.

Mienis, F., De Stigter, H.C., De Haas, H., Van Der Land, C. & Van Weering, T.C.E. (2012) Hydrodynamic conditions in a cold-water coral mound area on the Renard Ridge, southern Gulf of Cadiz. *Journal of Marine Systems*, *96–97*, 61–71.

Millot, C., Candela, J., Fuda, J.-L. & Tber, Y. (2006) Large warming and salinification of the Mediterranean outflow due to changes in its composition. *Deep Sea Research Part I: Oceanographic Research Papers*, *53*, 656–666.

Miramontes, E., Cattaneo, A., Jouet, G., Théreau, E., Thomas, Y., Rovere, M., Cauquil, E. & Trincardi, F. (2016) The Pianosa contourite depositional system (Northern Tyrrhenian Sea): drift morphology and Plio-Quaternary stratigraphic evolution. *Marine Geology*, *378*, 20–42.

Montero-Serrano, J.-C., Frank, N., Colin, C., Wienberg, C. & Eisele, M. (2011) The climate influence on the mid-depth Northeast Atlantic gyres viewed by cold-water corals. *Geophysical Research Letters*, *38*, L19604.

Nelson, H.C., Baraza, J. & Maldonado, A. (1993) Mediterranean undercurrent sandy contourites, Gulf of Cadiz, Spain. *Sedimentary Geology*, *82*, 103–131.

Pahnke, K. & Zahn, R. (2005) Southern hemisphere water mass conversion linked with North Atlantic climate variability. *Science*, *307*, 1741–1746.

Pahnke, K., Goldstein, S.L. & Hemming, S.R. (2008) Abrupt changes in Antarctic Intermediate Water circulation over the past 25,000 years. *Nature Geoscience*, *1*, 870–874.

Pardo-Iguzquiza, E. & Rodríguez-Tovar, F.J. (2011) Implemented Lomb-Scargle periodogram: a valuable tool for improving cyclostratigraphic research on unevenly sampled deep-sea stratigraphic sequences. *Geo-Marine Letters*, *31*, 537–545.

Pelegrí, J.L., Arístegui, J., Cana, L., González-Dávila, M., Hernández-Guerra, A., Hernández-León, S., Marrero-Díaz, A., Montero, M.F., Sangrà, P. & Santana-Casiano, M. (2005) Coupling between the open ocean and the coastal upwelling region off northwest Africa: water recirculation and offshore pumping of organic matter. *Journal of Marine Systems*, *54*, 3–37.

Peliz, Á., Dubert, J., Santos, A.M.P., Oliveira, P.B. & Le Cann, B. (2005) Winter upper ocean circulation in the Western Iberian Basin—Fronts, Eddies and Poleward Flows: an overview. *Deep Sea Research Part I: Oceanographic Research Papers*, *52*, 621–646.

Penaud, A., Eynaud, F., Turon, J.L., Blamart, D., Rossignol, L., Marret, F., Lopez-Martinez, C., Grimalt, J.O., Malaizé, B. & Charlier, K. (2010) Contrasting paleoceanographic conditions off Morocco during Heinrich events (1 and 2) and the Last Glacial Maximum. *Quaternary Science Reviews*, *29*, 1923–1939.

Penaud, A., Eynaud, F., Voelker, A., Kageyama, M., Marret, F., Turon, J.L., Blamart, D., Mulder, T. & Rossignol, L. (2011) Assessment of sea surface temperature changes in the Gulf of Cadiz during the last 30 ka: implications for glacial changes in the regional hydrography. *Biogeosciences*, *8*, 2295–2316.

Perez-Garcia, C., Berndt, C., Klaeschen, D., Mienert, J., Haffert, L., Depreiter, D. & Haeckel, M. (2011) Linked halokinesis and mud volcanism at the Mercator mud volcano, Gulf of Cadiz. *Journal of Geophysical Research: Solid Earth*, *116*, n/a-n/a.

Prins, M.A., Weltje, G.J., Harbaugh, J.W., Watney, W.L., Rankey, E.C., Slingerland, R., Goldstein, R.H. & Franseen, E.K. (1999) End-member modeling of siliciclastic grain-size distributions: the Late Quaternary Record of Eolian and fluvial sediment supply to the Arabian Sea and its paleoclimatic significance. In: *Numerical Experiments in Stratigraphy: Recent Advances in Stratigraphic and Sedimentologic Computer Simulations*. Tulsa: SEPM Society for Sedimentary Geology.

Prins, M.A., Postma, G., Cleveringa, J., Cramp, A. & Kenyon, N.H. (2000) Controls on terrigenous sediment supply to the Arabian Sea during the late Quaternary: the Indus Fan. *Marine Geology*, *169*, 327–349.

Rahmstorf. (2006) Thermohaline ocean circulation. In: Elias, S.A. (Ed.) *Encyclopedia of quaternary sciences*. Amsterdam: Elsevier.

Rebesco, M., Hernández-Molina, F.J., Van Rooij, D. & Wåhlin, A. (2014) Contourites and associated sediments controlled by deep-water circulation processes: State of the art and future considerations. *Marine Geology*, *352*, 111–154.

Reimer, P.J., Bard, E., Bayliss, A., Beck, J.W., Blackwell, P.G., Ramsey, C.B., Buck, C.E., Cheng, H., Edwards, R.L., Friedrich, M., Grootes, P.M., Guilderson, T.P., Haflidason, H., Hajdas, I., Hatté, C., Heaton, T.J., Hoffmann, D.L., Hogg, A.G., Hughen, K.A., Kaiser, K.F., Kromer, B., Manning, S.W., Niu, M., Reimer, R.W., Richards, D.A., Scott, E.M., Southon, J.R., Staff, R.A., Turney, C.S.M. & Van Der Plicht, J. (2013) IntCal13 and marine13 radiocarbon age calibration curves 0–50,000 years cal BP. *Radiocarbon*, *55*, 1869–1887.

Richardson, P.L., Bower, A.S. & Zenk, W. (2000) A census of Meddies tracked by floats. *Progress in Oceanography*, *45*, 209–250.

Rodrigo-Gámiz, M., Martínez-Ruiz, F., Rodríguez-Tovar, F.J., Jiménez-Espejo, F.J. & Pardo-Igúzquiza, E. (2014) Millennial- to centennial-scale climate periodicities and forcing mechanisms in the westernmost Mediterranean for the past 20,000 yr. *Quaternary Research*, *81*, 78–93.

Rogerson, M., Rohling, E.J., Weaver, P.P.E. & Murray, J.W. (2004) The Azores front since the last glacial maximum. *Earth and Planetary Science Letters*, *222*, 779–789.

Rogerson, M., Weaver, P.P.E., Rohling, E.J., Lourens, L.J., Murray, J.W. & Hayes, A. (2006) Colour logging as a tool in high-resolution palaeoceanography. *Geological Society, London, Special Publications*, *267*, 99–112.

Rogerson, M., Rohling, E.J., Bigg, G.R. & Ramirez, J. (2012) Paleoceanography of the Atlantic-Mediterranean exchange: Overview and first quantitative assessment of climatic forcing. *Reviews of Geophysics*, *50*, RG2003.

Röhl, U. & Abrams, L.J. (2000) High-resolution, downhole, and nondestructive core measurements from sites 999 and 1001 in the Caribbean Sea: Application to the late Paleocene thermal maximum. In: Leckie, R.M., Sigurdsson, H., Acton, G.D. & Draper, G. (Eds.) *Proceedings of the ODP, Scientific Results*.

Scargle, J.D. (1982) Studies in astronomical time series analysis. II. Statistical aspects of spectral analysis of unevenly spaced data. *The Astrophysical Journal*, *263*, 835.

Shackleton, N.J., Hall, M.A. & Vincent, E. (2000) Phase relationships between millennial-scale events 64,000–24,000 years ago. *Paleoceanography*, *15*, 565–569.

Skinner, L.C., Fallon, S., Waelbroeck, C., Michel, E. & Barker, S. (2010) Ventilation of the deep southern ocean and deglacial CO_2 rise. *Science*, *328*, 1147–1151.

Stow, D.A.V. & Faugères, J.C. (2008) Chapter 13 contourite facies and the facies model. In: Rebesco, M. & Camerlenghi, A. (Eds.) *Developments in Sedimentology*. Amsterdam: Elsevier.

Stow, D.A.V., Faugères, J.-C., Howe, J.A., Pudsey, C.J. & Viana, A.R. (2002) Bottom currents, contourites and deep-sea sediment drifts: current state-of-the-art. *Geological Society, London, Memoirs*, *22*, 7–20.

Stow, D.A.V., Hernández-Molina, F.J., Llave, E., Sayago-Gil, M., Díaz Del Río, V. & Branson, A. (2009) Bedform-velocity matrix: The estimation of bottom current velocity from bedform observations. *Geology*, *37*, 327–330.

Stow, D.A.V., Hernández-Molina, F.J., Llave, E., Bruno, M., García, M., Díaz Del Rio, V., Somoza, L. & Brackenridge, R.E. (2013) The Cadiz Contourite Channel: Sandy contourites, bedforms and dynamic current interaction. *Marine Geology*, *343*, 99–114.

Stuut, J.-B., Zabel, M., Ratmeyer, V., Helmke, P., Schefuß, E., Lavik, G. & Schneider, R. (2005) Provenance of present-day Eolian dust collected off NW Africa. *Journal of Geophysical Research: Atmospheres*, *110*, D04202.

Takashimizu, Y., Kawamura, R., Rodríguez-Tovar, F.J., Dorador, J., Ducassou, E., Hernández-Molina, F.J., Stow, D.A.V. & Alvarez-Zarikian, C.A. (2016) Reworked tsunami deposits by bottom currents: Circumstantial evidences from Late Pleistocene to Early Holocene in the Gulf of Cádiz. *Marine Geology*, *377*, 95–109.

Tallobre, C., Loncke, L., Bassetti, M.-A., Giresse, P., Bayon, G., Buscail, R., De Madron, X.D., Bourrin, F., Vanhaesebroucke, M. & Sotin, C. (2016) Description of a contourite depositional system on the Demerara Plateau: Results from geophysical data and sediment cores. *Marine Geology*, *378*, 56–73.

Thiem, Ø., Ravagnan, E., Fosså, J.H. & Berntsen, J. (2006) Food supply mechanisms for cold-water corals along a continental shelf edge. *Journal of Marine Systems*, *60*, 207–219.

Thornalley, D.J.R., Barker, S., Broecker, W.S., Elderfield, H. & Mccave, I.N. (2011) The deglacial evolution of North Atlantic deep convection. *Science*, *331*, 202–205.

Tjallingii, R., Röhl, U., Kölling, M. & Bickert, T. (2007) Influence of the water content on X-ray fluorescence core-scanning measurements in soft marine sediments. *Geochemistry, Geophysics, Geosystems*, *8*.

Tjallingii, R., Claussen, M., Stuut, J.-B.W., Fohlmeister, J., Jahn, A., Bickert, T., Lamy, F. & Röhl, U. (2008) Coherent high- and low-latitude control of the northwest African hydrological balance. *Nature Geoscience*, *1*, 670–675.

Tjallingii, R., Stattegger, K., Wetzel, A. & Van Phach, P. (2010) Infilling and flooding of the Mekong River incised valley during deglacial sea-level rise. *Quaternary Science Reviews*, *29*, 1432–1444.

Toucanne, S., Mulder, T., Schönfeld, J., Hanquiez, V., Gonthier, E., Duprat, J., Cremer, M. & Zaragosi, S. (2007) Contourites of the Gulf of Cadiz: A high-resolution record of the paleocirculation of the Mediterranean outflow water during the last 50,000 years. *Palaeogeography, Palaeoclimatology, Palaeoecology*, *246*, 354–366.

Van Rensbergen, P., Depreiter, D., Pannemans, B., Moerkerke, G., Van Rooij, D., Marsset, B., Akhmanov, G., Blinova, V., Ivanov, M., Rachidi, M., Magalhaes, V., Pinheiro, L., Cunha, M. & Henriet, J.-P. (2005) The El Arraiche mud volcano field at the Moroccan Atlantic slope, Gulf of Cadiz. *Marine Geology*, *219*, 1–17.

Van Rooij, D., Versteeg, W. & T. C. I. S. S. Party. (2005) *Cruise report Belgica 05/12 "CADIPOR II", Gulf of Cadiz, off Larache*. Morocco: RCMG Internal Publication, p. 43.

Van Rooij, D., Blamart, D. & Scientists, T. M. S. (2008) Cruise report MD169 MiCROSYSTEMS Brest (FR)-Algeciras (SP) 15–25 July 2008 ESF EURODIVERSITY MiCROSYSTEMS internal report.

Van Rooij, D., Blamart, D., De Mol, L., Mienis, F., Pirlet, H., Wehrmann, L.M., Barbieri, R., Maignien, L., Templer, S.P., De Haas, H., Hebbeln, D., Frank, N., Larmagnat, S., Stadnitskaia, A., Stivaletta, N., Van Weering, T., Zhang, Y., Hamoumi, N., Cnudde, V., Duyck, P. & Henriet, J.P. (2011) Cold-water coral mounds on the Pen Duick Escarpment, Gulf of Cadiz: the MiCROSYSTEMS project approach. *Marine Geology*, *282*, 102–117.

Vanderplas, J.T. (2018) Understanding the Lomb–Scargle Periodogram. *The Astrophysical Journal: Supplement Series*, *236*.

Vandorpe, T., Van Rooij, D. & De Haas, H. (2014) Stratigraphy and paleoceanography of a topography-controlled contourite drift in the Pen Duick area, southern Gulf of Cádiz. *Marine Geology*, *349*, 136–151.

Vandorpe, T., Martins, I., Vitorino, J., Hebbeln, D., García, M. & Van Rooij, D. (2016) Bottom currents and their influence on the sedimentation pattern in the El Arraiche Mud Volcano Province, southern Gulf of Cadiz. *Marine Geology*, *378*, 114–126.

Vandorpe, T., Wienberg, C., Hebbeln, D., Van Den Berghe, M., Gaide, S., Wintersteller, P. & Van Rooij, D. (2017) Multiple generations of buried cold-water coral mounds since the Early-Middle Pleistocene Transition in the Atlantic Moroccan Coral Province, southern Gulf of Cádiz. *Palaeogeography, Palaeoclimatology, Palaeoecology*, *485*, 293–304.

Vitorino, J., Martins, I., Carvalho, V., Esteves, R. & Marreiros, R. (2010) Physical properties affecting the Moroccan slope and the El-Arraiche MV field. Hermione Annual Meeting, Malta.

Voelker, A.H.L., Lebreiro, S.M., Schönfeld, J., Cacho, I., Erlenkeuser, H. & Abrantes, F. (2006) Mediterranean outflow strengthening during northern hemisphere coolings: a salt source for the glacial Atlantic? *Earth and Planetary Science Letters*, *245*, 39–55.

Waelbroeck, C., Lougheed, B.C., Vazquez Riveiros, N., Missiaen, L., Pedro, J., Dokken, T., Hajdas, I., Wacker, L., Abbott, P., Dumoulin, J.-P., Thil, F., Eynaud, F., Rossignol, L., Fersi, W., Albuquerque, A.L., Arz, H., Austin, W.E.N., Came, R., Carlson, A.E., Collins, J.A., Dennielou, B., Desprat, S., Dickson, A., Elliot, M., Farmer, C., Giraudeau, J., Gottschalk, J., Henderiks, J., Hughen, K., Jung, S., Knutz, P., Lebreiro, S., Lund, D.C., Lynch-Stieglitz, J., Malaizé, B., Marchitto, T., Martínez-Méndez, G., Mollenhauer, G., Naughton, F., Nave, S., Nürnberg, D., Oppo, D., Peck, V., Peeters, F.J.C., Penaud, A., Portilho-Ramos, R.D.C., Repschläger, J., Roberts, J., Rühlemann, C., Salgueiro, E., Sanchez Goni, M.F., Schönfeld, J., Scussolini, P., Skinner, L.C., Skonieczny, C., Thornalley, D., Toucanne, S., Van Rooij, D., Vidal, L., Voelker, A.H.L., Wary, M., Weldeab, S. & Ziegler, M. (2019) Consistently dated Atlantic sediment cores over the last 40 thousand years. *Scientific Data*, *6*, 165.

Wainer, I., Goes, M., Murphy, L.N. & Brady, E. (2012) Changes in the intermediate water mass formation rates in the global ocean for the last glacial maximum, mid-Holocene and pre-industrial climates. *Paleoceanography*, *27*, PA3101.

Wehrmann, L.M., Templer, S.P., Brunner, B., Bernasconi, S.M., Maignien, L. & Ferdelman, T.G. (2011) The imprint of methane seepage on the geochemical record and early diagenetic processes in cold-water coral mounds on Pen Duick Escarpment, Gulf of Cadiz. *Marine Geology*, *282*, 118–137.

Weltje, G.J. (1997) End-member modeling of compositional data: Numerical-statistical algorithms for solving the explicit mixing problem. *Mathematical Geology*, *29*, 503–549.

Weltje, G.J. & Tjallingii, R. (2008) Calibration of XRF core scanners for quantitative geochemical logging of sediment cores: Theory and application. *Earth and Planetary Science Letters*, *274*, 423–438.

Wienberg, C. & Titschack, J. (2017) Framework-forming Scleractinian cold-water corals through space and time: a Late Quaternary North Atlantic perspective. In: Rossi, S., Bramanti, L., Gori, A. & Orejas, C. (Eds.) *Marine animal forests: The ecology of Benthic biodiversity hotspots*. Switzerland: Springer International Publishing.

Wienberg, C., Hebbeln, D., Fink, H.G., Mienis, F., Dorschel, B., Vertino, A., Correa, M.L. & Freiwald, A. (2009) Scleractinian cold-water corals in the Gulf of Cádiz—First clues about their spatial and temporal distribution. *Deep Sea Research Part I: Oceanographic Research Papers*, *56*, 1873–1893.

Wienberg, C., Frank, N., Mertens, K.N., Stuut, J.-B., Marchant, M., Fietzke, J., Mienis, F. & Hebbeln, D. (2010) Glacial cold-water coral growth in the Gulf of Cádiz: Implications of increased palaeoproductivity. *Earth and Planetary Science Letters*, *298*, 405–416.

Zhang, W., Hanebuth, T.J.J. & Stöber, U. (2016) Short-term sediment dynamics on a meso-scale contourite drift (off NW Iberia): Impacts of multi-scale oceanographic processes deduced from the analysis of mooring data and numerical modelling. *Marine Geology*, *378*, 81–100.

Zitellini, N., Gràcia, E., Matias, L., Terrinha, P., Abreu, M.A., Dealteriis, G., Henriet, J.P., Dañobeitia, J.J., Masson, D.G., Mulder, T., Ramella, R., Somoza, L. & Diez, S. (2009) The quest for the Africa-Eurasia plate boundary west of the Strait of Gibraltar. *Earth and Planetary Science Letters*, *280*, 13–50.

SUPPORTING INFORMATION

Additional supporting information can be found online in the Supporting Information section at the end of this article.

How to cite this article: Vandorpe, T., Delivet, S., Blamart, D., Wienberg, C., Bassinot, F., Mienis, F., Stuut, J-B. & Van Rooij, D. (2023). Palaeoceanographic and hydrodynamic variability for the last 47 kyr in the southern Gulf of Cádiz (Atlantic Moroccan margin): Sedimentary and climatic implications. *The Depositional Record*, *9*, 30–51. https://doi.org/10.1002/dep2.212